

RESEARCH ARTICLE

Detection and attribution of precipitation trends associated with the poleward shift of the South Atlantic Convergence Zone using CMIP5 simulations

Marcia T. Zilli^{1,2}  | Leila M. V. Carvalho^{1,3}

¹Department of Geography, University of California, Santa Barbara, California

²School of Geography and the Environment, University of Oxford, Oxford, UK

³Earth Research Institute, University of California, Santa Barbara, California

Correspondence

Marcia T. Zilli, School of Geography and the Environment, University of Oxford, Oxford, OX1 3QY, UK.
Email: marcia.zilli@ouce.ox.ac.uk

Funding information

(CNPq); National Council for Scientific and Technological Development

Abstract

Observational studies demonstrate a poleward shift in the South Atlantic Convergence Zone (SACZ) in recent decades with regional impacts on extreme precipitation. However, the relative contribution of anthropogenic forcing and natural variability to the observed trends is presently unknown. To evaluate the main forcings associated with the recent trends in precipitation rate consistent with the poleward shift of the SACZ, this study examines the last 40 years of the historical scenario of 20 global climate models participating in the fifth phase of the Coupled Model Intercomparison Project (CMIP5). The relative contribution of natural variability and anthropogenic-related forcings to precipitation in the 20th century is assessed based on historical, natural, anthropogenic, and pre-industrial simulations from CMIP5 models. Over the study area, precipitation trends simulated by the CMIP5 historical scenario are small, with large disagreement among models and members. Despite the small magnitude of the trends, the spatial pattern emerging is coherent with a poleward displacement of the SACZ, as indicated by a reduction (increase) in the precipitation rate over Southeastern Brazil (Southeastern South America). Even with large discrepancies among models, the attribution analysis suggests that precipitation trends could partially result from land-use change, followed by changes in ozone concentrations, with more significant influence over Southeastern Brazil. The large uncertainty in the simulated precipitation suggests that not all mechanisms related to the position and intensity of the SACZ events are well captured by the CMIP5 models considered here.

KEYWORDS

anthropogenic forcing, CMIP5 models, natural variability, precipitation trend, South Atlantic Convergence Zone

1 | INTRODUCTION

The austral summer (December–February, DJF) precipitation over tropical South America (SA) is strongly linked

to the South American Monsoon System (SAMS) and the South Atlantic Convergence Zone (SACZ; Zhou and Lau, 1998; Barros *et al.*, 2000; Zhou and Lau, 2001; Carvalho *et al.*, 2004; 2011; Vera *et al.*, 2006a; Muza *et al.*, 2009).

This is an open access article under the terms of the Creative Commons Attribution License, which permits use, distribution and reproduction in any medium, provided the original work is properly cited.

© 2021 The Authors. International Journal of Climatology published by John Wiley & Sons Ltd on behalf of the Royal Meteorological Society.

The SACZ is a diagonal convergence zone extending from the Amazon toward west South Atlantic Ocean and is responsible for advecting moisture to the subtropical SA (Kodama, 1992; 1993; Zhou and Lau, 1998; Liebmann *et al.*, 2001; Carvalho *et al.*, 2002; 2004; Marengo *et al.*, 2012). It is characterized by the convergence of low-level northerly inflow originating along the western periphery of the South Atlantic Subtropical High (SASH) and westerly flows along the convergence zone, increasing in intensity with height and forming part of the subtropical jet in upper levels (Kodama, 1992; 1993).

The spatial variability of the SACZ is dominated by a dipole-like pattern of opposing precipitation anomalies over Eastern Brazil (EBr) and Southeastern South America (SESA), recurrent on timescales ranging from intra-seasonal to decadal (Nogues-Paegle and Mo, 1997; Zhou and Lau, 1998; Nogués-Paegle *et al.*, 2000; Carvalho *et al.*, 2002; 2011; Cunningham and Cavalcanti, 2006; Grimm and Zilli, 2009; Grimm and Saboia, 2015). During the SACZ active phase, precipitation is enhanced (inhibited) over EBr (SESA); the opposite is observed during its inactive phase (Zhou and Lau, 1998; Nogués-Paegle *et al.*, 2000; Carvalho *et al.*, 2002; Jones and Carvalho, 2002; Grimm and Zilli, 2009). On intraseasonal timescales, the SACZ circulation and convective activity are modulated by the Madden-Julian Oscillation (MJO) and by the Pacific South America (PSA) mode (Mo and Nogues-Paegle, 2001; Carvalho *et al.*, 2004; 2011; Cunningham and Cavalcanti, 2006).

On decadal timescales, the dipole is partially influenced by the Interdecadal Pacific Oscillation (IPO) and the Atlantic Multidecadal Oscillation (AMO; Grimm and Saboia, 2015; Jones and Carvalho, 2018). Previous studies suggest that during AMO positive (negative) phase, cold (warm) sea surface temperature anomalies over South Atlantic Ocean reduce (increase) the intensity of cyclones over the region (Kayano *et al.*, 2019), which in turn decrease (increase) the SACZ activity, reducing precipitation over EBr (Chiessi *et al.*, 2009; Bombardi *et al.*, 2013). Moreover, Jones and Carvalho (2018) have shown that the AMO modulates the decadal-to-multidecadal activity of the South American Low-Level Jet (LLJ), with the negative AMO phase related to enhanced precipitation over Paraguay, southern Brazil, and northern Argentina, favouring the inactive phase of the SACZ-dipole. However, this same study showed that the differences in precipitation between AMO phases are exacerbated in area and intensity when trends are not removed, suggesting that the AMO cannot explain the complete variability in rainfall in the SACZ domain.

The increase in low tropospheric temperatures over the SA during the last decades of the 20th century has been consistently shown in reanalyses and global climate models (GCM) contributing to the fifth phase of the

Coupled Model Intercomparison Project (CMIP5). Models and observations agree that trends are larger over central-eastern Brazil (Carvalho and Jones, 2013; de Barros Soares *et al.*, 2017). The rapid rate of warming cannot be explained by natural variability alone, suggesting that the contribution of anthropogenic-related forcings is already detectable (de Barros Soares *et al.*, 2017). As expected for a warmer troposphere, the water vapour content is also increasing, particularly over the regions with larger warming (Carvalho and Jones, 2013) with implications for duration and amplitude of the SAMS (Jones and Carvalho, 2013).

Observational studies (Zilli *et al.*, 2017; 2019) and historical and future scenarios of CMIP3 and CMIP5 models simulations (Seth *et al.*, 2010; Junquas *et al.*, 2012; Jones and Carvalho, 2013; Díaz and Vera, 2017) identified evidence of changes in the SACZ-related dipole. Using future changes in sea surface temperature (SST) derived from the CMIP3 model ensemble to force a Regional Climate Model (RCM) interactively coupled (i.e., using a two-way nesting technique) to an Atmospheric Global Climate Model (AGCM), Junquas *et al.* (2013) demonstrated a prevalence of SACZ inactive phase as a response to an asymmetric increase in SST over the Indian and equatorial western Pacific. The asymmetric equatorial warming generates a Rossby wave-train pattern that propagates toward South America, favouring cyclonic (anticyclonic) anomalies and consequent increase (decrease) in precipitation over SESA (SACZ).

The increase in total precipitation over SESA, the subtropical portion of the SACZ dipole, has been identified in observational studies and is mostly related to an increase in the number of intense events and a reduction in the number of consecutive dry days over the region (Haylock *et al.*, 2006; Barros *et al.*, 2008; Skansi *et al.*, 2013; Zilli *et al.*, 2017; 2019). These trends, as well as the precipitation climatology over the region, are correctly reproduced by historical scenarios of coupled GCMs and RCM models (Vera *et al.*, 2006b; Chou *et al.*, 2014; Díaz and Vera, 2017) and have been attributed to the anthropogenic-related increase in the concentration of well-mixed greenhouse gases (Zhang *et al.*, 2016) and stratospheric ozone depletion (Polvani *et al.*, 2011; Gonzalez *et al.*, 2014).

Previous observational studies also detected negative trends in precipitation over EBr, the tropical portion of the SACZ dipole (Zilli *et al.*, 2017; 2019). Zilli *et al.* (2017) detected changes in the observed precipitation distribution over Southeastern Brazil, with fewer rainy days and more intense events observed in recent decades along the northern margin of the SACZ during the rainy season (October to March). Zilli *et al.* (2019) related the reduction in precipitation rate over EBr to the weakening of the northerly winds and decrease in the available

moisture at the mid-to-lower troposphere (700 hPa) co-located with the climatological position of the SASH. These changes in circulation and low-level moisture have reduced convergence and moisture advected to EBr. Using an Atmospheric Global Climate Model (AGCM), Talento and Barreiro (2017) identified negative precipitation trends and related circulation changes over tropical Brazil as a response to extratropical warming over the northern hemisphere, similar to the atmospheric warming observed over the last decades. The hemispheric warming has been associated with changes in the Hadley circulation, resulting in weakened trade winds along the equator and enhanced SASH, increasing subsidence over the northern margin of the SACZ. Together with the well-documented positive precipitation trends over SESA, these results suggest a poleward shift in the SACZ position over recent decades (Zilli *et al.*, 2019). However, there are significant discrepancies among the CMIP5 historical and future projections over the region, typically because the models do not accurately reproduce the precipitation variability related to the SACZ position, intensity and seasonal variability (Carvalho and Jones, 2013; de Barros Soares *et al.*, 2017; Díaz and Vera, 2017).

The objective of this study is to evaluate the contribution of natural variability and anthropogenic-related forcings to precipitation trends in the SACZ-related dipole, associated with a poleward shift of the convergence zone in the 20th century. The attribution analysis is conducted using single forcing scenarios from the CMIP5 archive. Challenges due to large uncertainties related to the climate system internal variability and models' representation of the climate system are accounted for by evaluating multiple CMIP5 ensemble members. This study is organized as follows: dataset and methodology are described in Section 2. The observed and simulated DJF precipitation climatology are presented in Section 3. Section 4 discusses the trends in recent decades, while Section 5 focuses on the attribution analysis, emphasizing the influence of natural internal variability and external forcings on the simulated trends. The main results are discussed in Section 6 and conclusions are presented in Section 7.

2 | DATA AND METHODS

2.1 | Data

This study compares precipitation trends simulated by CMIP5 climate models with those identified in observations. The observational dataset is from the Global Precipitation Climatology Project Version 2.3 (GPCP; Adler *et al.*, 2016; 2018), a monthly dataset with 2.5° lon/lat horizontal resolution and spanning 1979–2019. GPCP

merges directly observed precipitation from rain gauge over land with various satellite-based estimates (Adler *et al.*, 2018). Its previous version (GPCP V2.1) accurately reproduces the spatial and temporal precipitation variability related to the SAMS (Carvalho *et al.*, 2012).

The simulated precipitation is from various GCMs selected from the CMIP5 archive (Taylor *et al.*, 2012) available through the Program for Climate Model Diagnosis and Intercomparison (PCMDI). Precipitation trends are detected in the historical scenario (HIST) of 20 CMIP5 GCM, considering all available ensemble members (Table 1) and resulting in 76 simulations. The attribution analysis is based on the external forcing scenarios, divided into natural and anthropogenic-related. The external natural forcing influence is accessed through the natural scenario (NAT), in which the atmospheric composition is kept constant at pre-industrial levels and external forcings are only due to changes in incoming solar radiation and stratospheric aerosol from volcanic sources. The anthropogenic influence can be estimated using four single-forcing scenarios: anthropogenic-related changes in greenhouse gas concentration (GHG); anthropogenic aerosol emissions (AA), which may include direct and indirect effects; anthropogenic-related changes in tropospheric and stratospheric ozone concentration (OZ), and the influence of land-use changes (LU). Table 2 describes these scenarios and lists the models utilized in each case. A more in-depth discussion of these scenarios can be found in Taylor *et al.* (2012).

In addition to external forcings, simulated trends can ensue from natural internal variability intrinsic to the climate system, represented by climatic modes such as ENSO, AMO, IPO, among others. Here, we use the pre-industrial control run (PICONROL) as a proxy for this variability. In the PICONROL experiment, all external forcings are kept constant at pre-industrial levels, with the simulated precipitation variability and its trends related to interactions between the different components of the climate system (Taylor *et al.*, 2012).

The results described are based on the analysis of individual ensemble members of each model and scenario, their averages, which are referred to as Multi-Member Mean (MMeM), and the average of all MMeM, forming the Multi-Model Mean (MMoM) for each scenario. With this approach, each MMeM have the same weight in the MMoM, independent of their number of members.

2.2 | Precipitation trend detection

To analyse how CMIP5 models simulate the location and intensity of the SACZ, we compare the austral summer (December to February—DJF) average of daily precipitation rate (*PP*) and its trend (τ) from GPCP with respective

TABLE 1 CMIP5 models, institutes, resolution, and references

	Model	Institute and country	Resolution	Reference
A	ACCESS1-3	Centre for Australian Weather and Climate Research (CAWCR), Australia	1.875°×1.25° (N96)	Bi <i>et al.</i> (2013)
B	BCC-CSM1-1	Beijing Climate Center (BCC), China Meteorological Administration, China	1.89°×1.89° (T42L26)	Wu <i>et al.</i> (2013)
C	CanESM2	Canadian Centre for Climate Modelling and Analysis (CCCMA), Canada	2.8°×2.8° (T63L35)	Arora <i>et al.</i> (2011)
D	CCSM4	National Center for Atmospheric Research (NCAR), USA	1.25°×0.9° (F09G16)	Gent <i>et al.</i> (2011)
E	CMCC-CESM	Centro Euro-Mediterraneo per i Cambiamenti Climatici, Bologna, Italy	3.75°×3.75	Vichi <i>et al.</i> (2011)
F	CNRM-CM5	Centre National de Recherches Météorologiques (CNRM) and Centre Européen de Recherche et de Formation Avancée (CERFACS), France	1.4°×1.4° (TL127L31)	Voldoire <i>et al.</i> (2013)
G	CSIRO_Mk3-6-0	Centre for Australian Weather and Climate Research (CSIRO) and Queensland Climate Change Centre of Excellence, Australia	1.875°×1.875° (T63)	Jeffrey <i>et al.</i> (2013)
H	FGOALS-g2	Institute of Atmospheric Physics, Chinese Academy of Sciences, Beijing, China (IAP) and Tsinghua University (THU)	2.1825°×3.0° (L62)	Li <i>et al.</i> (2013)
I	GFDL-ESM2M	Geophysical Fluid Dynamics Laboratory, National Oceanic and Atmospheric Administration (GFDL/NOAA), USA	2.5°×2° (M45L24)	Dunne <i>et al.</i> (2012)
J	GISS-E2H	Goddard Institute for Space Studies, National Aeronautics and Space Administration (GISS/NASA), USA	2.5°×2.0°	Schmidt <i>et al.</i> (2014)
K	HadGEM2-CC	Met Office Hadley Centre, UK	1.875°×1.25° (N96L60)	Collins <i>et al.</i> (2011) Martin <i>et al.</i> (2011)
L	HadGEM2-ES	Met Office Hadley Centre, UK	1.875°×1.25° (N96L38)	Collins <i>et al.</i> (2011) Jones <i>et al.</i> (2011)
M	INMCM4	Institute for Numerical Mathematics (INM), Russia	2.0°×1.5°	Volodin <i>et al.</i> (2010)
N	IPSL-CM5A-LR	Institut Pierre Simon Laplace (IPSL), France	3.75°×1.875°	Dufresne <i>et al.</i> (2013)
O	MIROC4h	Atmosphere and Ocean Research Institute (AORI) of the University of Tokyo, National Institute for Environmental Studies (NIES), and Japan Agency for Marine-Earth Science and Technology (JAMSTEC), Japan	0.5625°×0.5625° (T213L56)	Sakamoto <i>et al.</i> (2012)
P	MIROC5	Atmosphere and Ocean Research Institute, The University of Tokyo, Chiba, Japan (AORI), National Institute for Environmental Studies, Ibaraki, Japan (NIES), Japan Agency for Marine-Earth Science and Technology, Kanagawa, Japan (JAMSTEC)	1.40625°×1.40625°	Watanabe <i>et al.</i> (2010)
Q	MIROC-ESM	Atmosphere and Ocean Research Institute (The University of Tokyo), National Institute for Environmental Research, and Japan Agency for Marine-Earth Science and Technology, Japan	2.8125°×2.8125° (T42L80)	Watanabe <i>et al.</i> (2011)
R	MPI-ESM-LR	Max Planck Institute for Meteorology (MPI-M), Germany	1.875°×1.875° (T63L47)	Giorgetta <i>et al.</i> (2013)
S	MRI-CGCM3	Meteorological Research Institute, Japan	1.125°×1.125° (TL159L48)	Yukimoto <i>et al.</i> (2012)
T	NorESM1-M	Norwegian Climate Centre (NorClim), Norway	2.5°×1.875° (F19L26)	Bentsen <i>et al.</i> (2013)

TABLE 2 Description of forcings related to and a list of models considered in each scenario

Scenario	Description	Models
PI control (PICONROL)	Pre-industrial conditions fixed at pre-industrial levels. May include prescribed atmospheric concentrations or non-evolving emissions, solar radiation, and unperturbed land use	All 20 models listed in Table 1, 76 members
Historical (HIST)	Simulation of the recent past (1850–2005), imposing observed natural and anthropogenic changes in atmospheric composition (such as GHG, as in GHG scenario, tropospheric and stratospheric ozone (Oz), direct and indirect effects of anthropogenic sulfate aerosol (SA), black carbon (BC), organic carbon (OC), solar radiation (SI), volcanic aerosol (VI), mineral dust (MD), sea salt (SS)) and land use	All 20 models listed in Table 1, 76 members
Natural (NAT)	Recent past (1850–2005) observed variations in solar radiation (SI) and volcanic aerosol (VI). Other forcings are fixed at pre-industrial levels	12 models, 42 members: ACCESS1-3; BCC-CSM1-1; CanESM2; CCSM4; CNRM-CM5; CSIRO_Mk3-6-0; GFDL-ESM2M; HadGEM2-ES; IPSL-CM5A-LR; MIROC-ESM; MRI-CGM3; NorESM1-M
GHG (GHG)	Recent past (1850–2005) observed GHG concentration: CO ₂ , N ₂ O, CH ₄ , CFC11, CFC12, CFC113, HCFC22, HFC125, and HFC134a	12 models, 41 members: ACCESS1-3; BCC-CSM1-1; CanESM2; CCSM4; CNRM-CM5; CSIRO_Mk3-6-0; GFDL-ESM2M; HadGEM2-ES; IPSL-CM5A-LR; MIROC-ESM; MRI-CGM3; NorESM1-M
Anthropogenic aerosols (AA)	Recent past (1850–2005) observed changes in anthropogenic aerosol concentration, which may include: Direct (SD) and indirect (SA) effects of anthropogenic sulfate aerosol, SS, dust (Ds), SD, BC, MD, OC. Other forcings are fixed at pre-industrial levels	5 models, 20 members: CanESM2; CCSM4; CSIRO_Mk3-6-0; GFDL-ESM2M; IPSL-CM5A-LR
Ozone (OZ)	Recent past (1850–2,205) changes in tropospheric and stratospheric ozone. Other forcings are fixed at pre-industrial levels	1 model, 2 members: CCSM4
Land use (LU)	Recent past (1850–2005) observed land use change. Other forcings are fixed at pre-industrial levels	3 models, 8 members: CanESM2; CCSM4; GFDL-ESM2M

PP and τ from all 20 CMIP5 models. Note that the DJF PP of a specific year is calculated using December of that year and January and February of the next year. For the observational dataset (GPCP), the statistics are calculated between 1979 and 2019 and between 1979 and 2005, covering the overlapping period of historical CMIP5 data; for CMIP5 models we considered the last 40 years of the historical scenario (1966–2005) so both series have the same length. Despite covering different periods, having observational and simulated time series with the same length result in more reliable statistics when comparing trends using non-parametric tests such as the Mann–Kendall (Wilks, 2011). The caveat of this approach is that it excludes the period after 2005 from the simulated dataset, which could result in underestimated trends. Other

options, such as using CMIP5 future projections after 2005 would increase the uncertainties of the results.

All CMIP5 data (including PICONROL) are interpolated to GPCP 2.5° resolution using linear interpolation. Trends in all datasets and scenarios are estimated based on Mann–Kendall (Wilks, 2011) and Sen's Slope (Sen, 1968) tests, as described in Zilli *et al.* (2017). The Sen's slope measures the magnitude of the trend (τ) in all datasets and the Mann Kendall test indicates the areas where trends are statistically significant ($p < 0.1$). As the main goal of this study is to investigate changes in precipitation resulting from changes in the SACZ position, the evaluation criteria are based on the spatial representation of PP and τ over Southeastern Brazil, (SEBr; brown box in Figure 1) and SESA (green box in Figure 1). These two

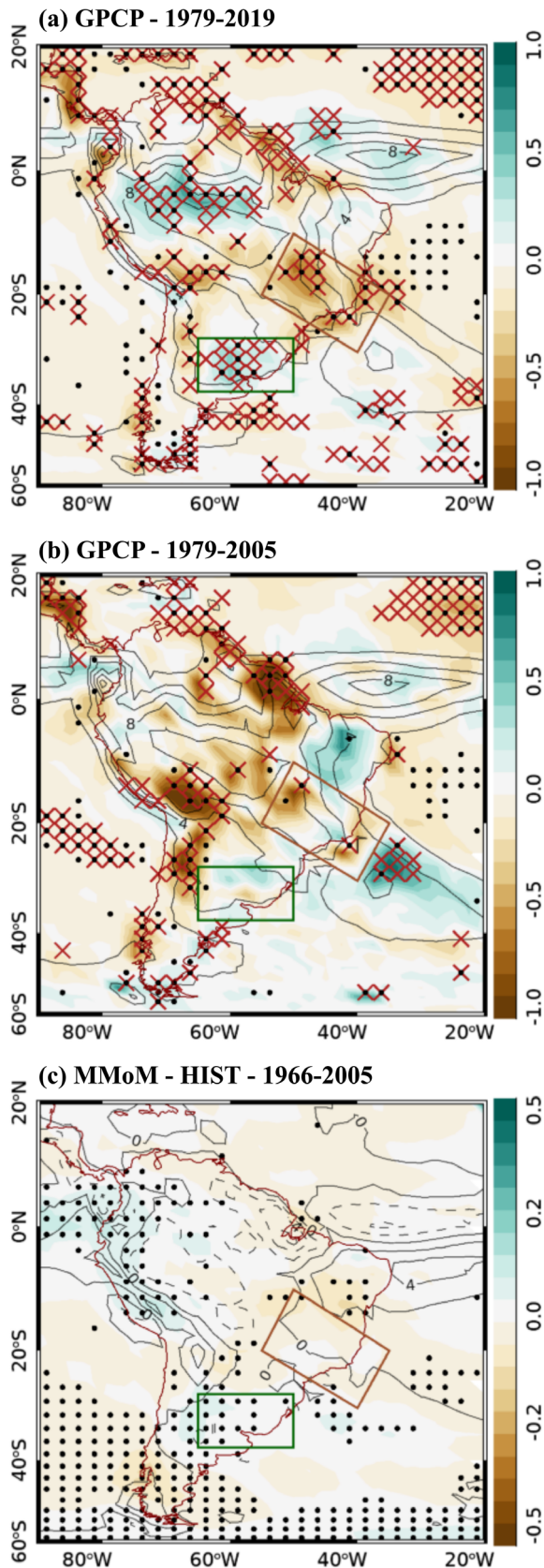


FIGURE 1 Legend on next column.

regions represent the main centres of action of the SACZ-related dipole. The pattern analysis metrics considered are the Root Mean Square Error ($RMSE$) and uncentered regression coefficient (R) obtained with respect to GPCP.

The $RMSE$ is calculated according to Taylor (2001):

$$RMSE = \sqrt{\sigma_o^2 + \sigma_s^2 - 2\sigma_o\sigma_s\rho} \quad (1)$$

where σ_o and σ_s are the spatial standard deviation of the GPCP (observed—"o" index) and CMIP5 (simulated—"s" index) statistics, respectively. ρ is the spatial correlation between the observed and simulated datasets and is calculated as:

$$\rho = \frac{\sum_{i=1}^{NP} W_i (x_{i,o} - \mu_o)(x_{i,s} - \mu_s)}{\sum_{i=1}^{NP} W_i (x_{i,o} - \mu_o)^2 \sum_{i=1}^{NP} W_i (x_{i,s} - \mu_s)^2} \quad (2)$$

where x_i is either PP (in $\text{mm}\cdot\text{day}^{-1}$) or τ (in $\text{mm}\cdot\text{day}^{-1}\cdot 10\text{ yr}^{-1}$) at each $i = 1, \dots, NP$ grid points in the considered study region, and μ is the spatial average over the area. W_i is the spatial weight, calculated as $(1/\cos\varphi_i) / \sum_{i=1}^{NP} (1/\cos\varphi_i)$, where φ_i is the latitude of each grid point (in radians). The spatial standard deviation is calculated as:

$$\sigma = \sqrt{\frac{NP}{NP-1} \sum_{i=1}^{NP} W_i (x_i - \mu)^2} \quad (3)$$

and the areal average μ of each variable is:

$$\mu = \frac{\sum_{i=1}^{NP} W_i x_i}{NP} \quad (4)$$

FIGURE 1 PP (contours, each $2\text{ mm}\cdot\text{day}^{-1}$) and Sen's slope τ (shades, in $\text{mm}\cdot\text{day}^{-1}\cdot 10\text{ yr}^{-1}$) for GPCP DJF (a) 40-year period (1979–2019) and (b) 26-year period (1979–2005). (c) As in (a), for anomalies in PP for MMoM HIST scenario (1966–2005). Note reduced τ range in (c). Red cross-hatching indicates areas where the trends are distinguishable from internal natural variability while stippling indicates where the trends are statistically significant ($p < 0.1$) according to the Mann–Kendall trend test. Note that none of the grid points in (c) passed the PICONTR0L test. Brown (green) box represents the location of the study area over the SACZ (SESA) [Colour figure can be viewed at wileyonlinelibrary.com]

The uncentered spatial regression coefficient R (Hegerl and Zwiers, 2011; Barkhordarian *et al.*, 2012; 2013; Polson and Hegerl, 2017) is used to evaluate the similarity between the observed and simulated spatial patterns over the study areas. It can be defined as:

$$R = \frac{\sum_{i=1}^{NP} x_{i,o} x_{i,s}}{\sum_{i=1}^{NP} (x_{i,s})^2} \quad (5)$$

The R index indicates whether the co-variability between observations ($x_{i,o}$) and simulations ($x_{i,s}$), represented by the numerator in Equation (5), can be distinguished from the simulation variability, represented by the denominator in Equation (5). It measures the relative magnitude between observed and simulated trends (Barkhordarian *et al.*, 2012), with positive (negative) values of R indicating that they are similar (dissimilar). Values of R greater (smaller) than 1 indicate an underestimation (overestimation) of the trend by the simulations while $R = 1$ indicating a perfect simulation of the observed spatial patterns (Polson and Hegerl, 2017).

2.3 | Detection and attribution analysis

One of the advantages of using CMIP5 simulations to identify trends in climatic variables is the availability of the PICONTR0L, with simulations undisturbed by external forcings. Data from the PICONTR0L of all 20 CMIP5 models are averaged over austral summer (DJF) and interpolated to the GPCP 2.5° resolution. For each model, we remove the model's drift (Gupta *et al.*, 2013) by adjusting a linear regression to the entire time series before dividing them into non-overlapping 40-year periods. For each period, we estimate PP and τ , resulting in 251 independent realizations used to calculate the probability distribution and confidence intervals of the variables.

The analysis is divided into two parts: detection of trends in observed and historical simulation precipitation, and the attribution of the simulated trends to external forcings, represented by natural- and anthropogenic-forcing scenarios. In both cases, the PICONTR0L distribution is used to assess the similarity between observed and simulated trends and the influence of internal natural variability.

In the first part of the analysis, our objective is to identify whether the CMIP5 HIST simulations can correctly reproduce the observed precipitation rate and its trends. Simulated values of PP are considered similar to

the observed when they are within the confidence interval defined by the PICONTR0L. In the same way, the PICONTR0L distribution can also be considered as a confidence interval for the $RMSE$ and R similarity metrics (as defined by Equations (1) and (5), respectively). In this case, the probability distribution is estimated after calculating the $RMSE$ and R between PP from GPCP and each of the non-overlapping 40-year PICONTR0L intervals. Additionally, both observed and simulated τ are considered significantly different from those caused by natural internal variability when their statistics are outside the confidence intervals based on the PICONTR0L τ distribution.

The attribution analysis is based on the evaluation of the simulated τ in each scenario. In this part of the analysis, the objective is to identify the contribution of each forcing to the simulated τ , independently on its sign. The spatial pattern of the trends in a given scenario is considered significantly different from those caused by natural internal variability when the R between the scenario's and GPCP's τ is outside the confidence interval of the R distribution, obtained when regressing the simulated τ with each of the non-overlapping 40-year PICONTR0L intervals.

3 | CLIMATOLOGY

The GPCP climatology for DJF PP over SA (contours in Figure 1a, b) is characterized by the Intertropical Convergence Zone (ITCZ) over equatorial Atlantic and Pacific oceans and by the SAMS, with maximum seasonal averages over the central Amazon extending toward subtropical South Atlantic, forming the SACZ. These features are correctly reproduced by the MMoM of the HIST scenario, with the exception to the double ITCZ over equatorial Atlantic (contours in Figure 1c). Note that in Figure 1c, contours represent the MMoM's bias, that is, the difference between MMoM's and GPCP's PP .

In the MMoM HIST simulation, the maximum precipitation associated with the SACZ is located northward of its climatological position (Figure 1c), resulting in a positive (negative) bias in PP over the north (south) part of the SEBr study area (brown box in Figure 1c). Despite that, the spatial average (grey bars in Figure 2a) and standard deviation (red whiskers in Figure 2a) of PP over SEBr are well reproduced by the MMoM (see also values in Table 3). The spatial pattern of PP is similar to the GPCP's, with spatial correlation $\rho = 0.89$ (Table 3), which is larger than the 75th percentile of the probability distribution derived from the 251 non-overlapping 40-year periods from the PICONTR0L simulations. As a result, the $RMSE$ between HIST and GPCP is small ($=0.45$,

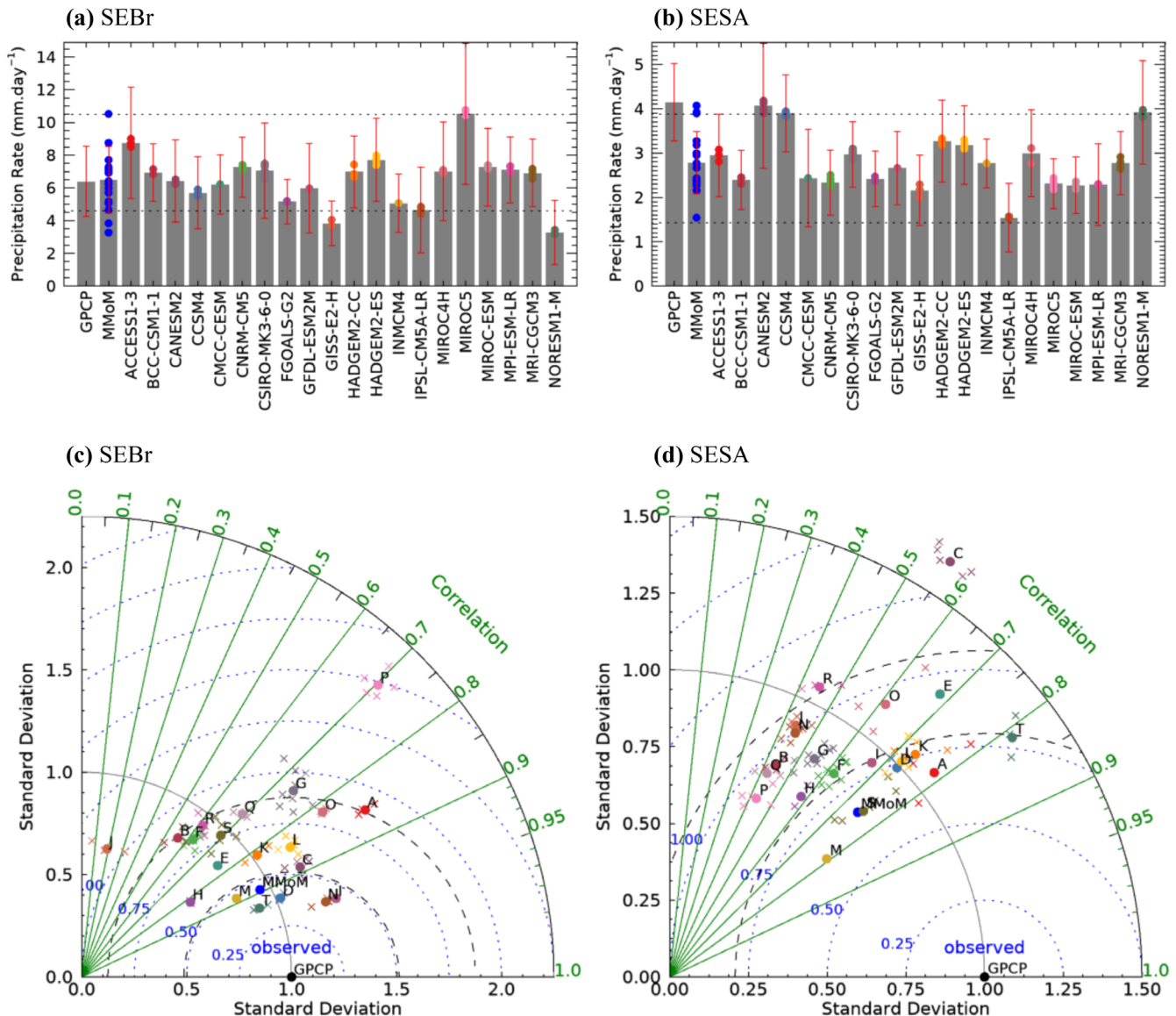


FIGURE 2 (a,b) Spatially averaged *PP* for GPCP, MMOM, each MMeM (bars), and individual members (dots; in MMOM bar dots represent each MMeM). Red bars with whiskers: Spatially averaged standard deviation for GPCP, MMOM, and each MMeM. Dotted line: 5th–95th confidence interval defined by the PICONTRON distribution. (c,d) Taylor diagram for spatially averaged *PP*, comparing GPCP values to HIST scenario of MMOM, each MMeM (dots), each member of MMeM ("x"). Dashed lines represent the interquartile range interval of the *RMSE* for the PICONTRON distribution. See Table 1 for the correspondence between letters and CMIP5 models. Values are averaged over (a) and (c) SEBr and (b) and (d) SESA [Colour figure can be viewed at wileyonlinelibrary.com]

Table 3 and Figure 2c) and below the 25th percentile of the PICONTRON distribution.

Over SESA (green box in Figure 1c), the MMOM HIST simulation is not as accurate, underestimating the spatially averaged *PP* and its standard deviation (Figure 2b and Table 3). Similar underestimation of the DJF precipitation by CMIP5 models has been identified in previous studies (Gulizia and Camilloni, 2015) and was related to underestimation in the southerly flow east of the Andes, responsible for advecting moisture from the Amazon region to the SESA (Barros and Doyle, 2018). Despite

that, the MMOM correctly simulates the *PP* spatial pattern, with ρ (*RMSE*) equal 0.74 (0.58) and in the upper (lower) quartile of the PICONTRON distribution (Table 3 and Figure 2d). It is interesting to notice that the observed *PP* is outside the interquartile range of *PP* simulated by the PICONTRON (represented by the dotted lines in Figure 2b).

Considering each MMeM individually, not all HIST simulations accurately reproduce the DJF average precipitation over SA, with the largest bias occurring over the Andes and the Amazon basin (contours in Figure 3).

TABLE 3 Spatial average (μ) of GPCP and each MMoM scenario, normalized standard deviation (σ/σ_{GPCP}), spatial correlation (ρ), and normalized RMSE (Equations (1)–(4)) with respect to GPCP for PP (in $\text{mm}\cdot\text{day}^{-1}$) and τ (in $\text{mm}\cdot\text{day}^{-1}\cdot 10\text{ yr}^{-1}$) calculated over the SEBr and SESA (brown and green boxes in Figure 1, respectively)

SCENARIO	PP ($\text{mm}\cdot\text{day}^{-1}$)				τ ($\text{mm}\cdot\text{day}^{-1}\cdot 10\text{ yr}^{-1}$)			
	SEBr				SEBr			
	μ	σ/σ_{GPCP}	ρ	RMSE	μ	σ/σ_{GPCP}	ρ	RMSE
GPCP	6.39	1.00	1.00	0.00	−0.32	1.00	1.00	0.00
HIST	6.49	0.95	0.89	0.45	−0.01	0.15	−0.04	1.02
NAT	6.59	1.00	0.92	0.40	−0.06	0.15	−0.04	1.02
GHG	6.72	1.04	0.92	0.42	0.05	0.21	0.12	1.00
AA	6.02	1.15	0.95	0.37	−0.05	0.25	0.01	1.03
OZ	6.04	1.06	0.93	0.40	−0.10	0.62	0.31	1.00
LU	6.19	1.11	0.95	0.34	−0.18	0.40	−0.09	1.11
SESA					SESA			
GPCP	4.14	1.00	1.00	1.00	0.13	1.00	1.00	0.00
HIST	2.78	0.80	0.74	0.58	0.03	0.11	0.06	1.00
NAT	2.77	0.79	0.75	0.58	0.02	0.16	0.33	0.96
GHG	2.92	0.82	0.78	0.55	0.01	0.11	−0.08	1.01
AA	2.81	0.86	0.71	0.62	0.02	0.20	0.08	1.00
OZ	3.70	0.85	0.75	0.58	0.02	0.32	−0.04	1.06
LU	3.26	1.01	0.73	0.65	0.06	0.35	0.27	0.97

Most of the selected models displace the maximum precipitation from the Amazon eastward/southeastward of the observed climatological position, overestimating precipitation over semi-arid northeastern Brazil. In previous studies, the dry bias over the Amazon has been related to overestimated precipitation over the ITCZ, changing the moisture flux to the Amazon and affecting the precipitation annual cycle (Bombardi and Carvalho, 2009; Yin *et al.*, 2013). This displacement is manifested in the MMoM HIST scenario as negative (positive) bias over the Amazon (Northeastern Brazil; Figure 1c). Five models fail in reproducing the spatial characteristics of SAMS precipitation, placing the maximum precipitation as a zonal band over the equator (CMCC-CESM, GISS-E2-H, INMCM4, and MPI-ESM-LR) or the subtropics (CSIRO-Mk3-6-0).

Over both study areas, most of the selected MMeM correctly simulated the average PP and its spatial pattern, with the spatial average of PP within the interquartile range of PP simulated by the PICONTR0L (Figure 2a,b) and their $RMSE$ below the 75th percentile of the probability distribution from the PICONTR0L (Figure 2c,d). Nonetheless, most MMeM displaces the maximum precipitation associated with the SACZ to the north part of SEBr (brown box in Figure 3), resulting in the bias observed in the MMoM. Over SEBr, the $RMSE$ between the observed and simulated spatial pattern of PP is below the 25th percentile of the PICONTR0L distribution (i.e., below 0.51, with this value represented as the innermost dashed black circle in Figure 2c) in 5 MMeM

(CCSM4, GFDL-ESM2M, INMCM4, IPSL-CM5A_LR, and NorESM1-M) suggesting a reliable representation of the precipitation rate in these MMeM. On the other hand, in 5 MMeM (ACCESS1-3, BCC-CSM1-1, CSIRO-Mk3-6-0, GISS-E2-H, and MIROC5), the $RMSE$ was above the upper quartile of the PICONTR0L distribution (i.e., below 0.87; outermost dashed black circle in Figure 2c), suggesting large discrepancies between observations and simulations.

Over SESA, all except two MMeM have $RMSE$ below the 75th percentile of the PICONTR0L distribution (CanESM2 and MPI-ESM-LR; Figure 2d) and in 8 MMeM, the $RMSE$ is below the 25th percentile of the PICONTR0L distribution (ACCESS1-3, CCSM4, GFDL-ESM2M, HadGEM2-CC, HadGEM2-ES, INMCM4, MRI-CGCM3, and NorESM1-M). In Figure 2 it is also evident the small spread of simulated PP (Figure 2a,b, dots) and respective $RMSE$ (Figure 2c,d, “x”) among members of each MMeM member.

Thus, the MMoM of the 20 selected models accurately simulates the magnitude of the precipitation rates averaged over the study regions (SEBr and SESA). However, the MMoM is not able to correctly reproduce the spatial location of the SACZ, with the maximum precipitation located to the north of its climatological location, affecting the SACZ-related dipole. Consequently, the MMeMs that better reproduce the precipitation rate over one study area may not be as accurate over the other (see Table 4). Nonetheless, the results obtained here are in agreement with previous studies, among them Cavalcanti

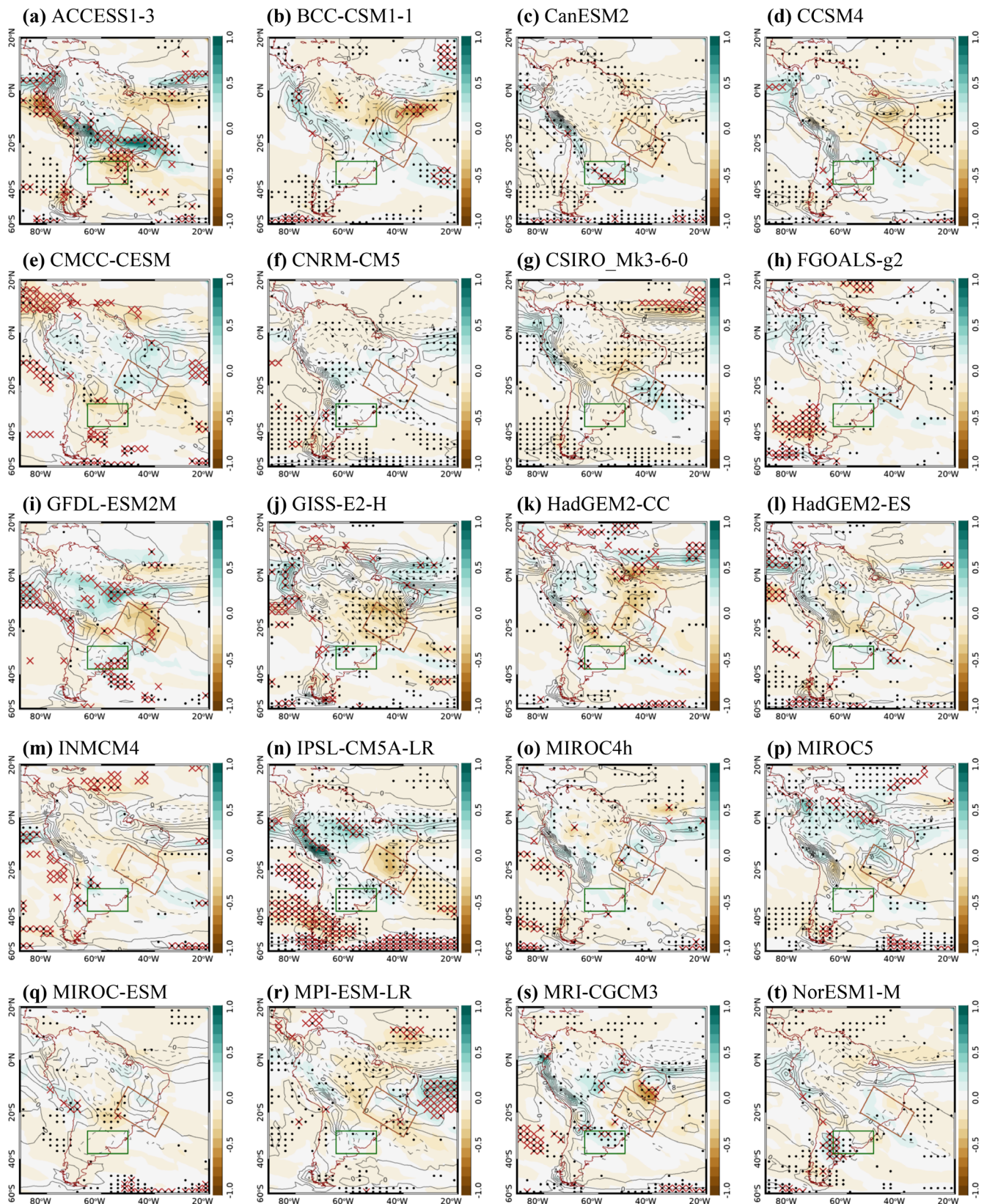


FIGURE 3 Anomalies of PP (in $\text{mm}\cdot\text{day}^{-1}$; contours each $2\text{ mm}\cdot\text{day}^{-1}$) and τ (in $\text{mm}\cdot\text{day}^{-1}\cdot 10\text{ yr}^{-1}$, shades) for MMeM models in the HIST scenario. Red cross-hatchings indicate areas where the trends are distinguishable from internal natural variability while stipplings indicate where τ is statistically significant ($p < 0.1$) according to the Mann-Kendall trend test. Brown (green) box represents the location of the study area over the SEBr (SESA) [Colour figure can be viewed at wileyonlinelibrary.com]

TABLE 4 PP columns: Simulations with *RMSE* below (above) the 75th percentile of the PICONTR0L distribution are shaded blue (red); crossed cells indicating *RMSE* below the 25th percentile of the PICONTR0L distribution

	SEBr							SESA						
	<i>PP</i>	τ_{HIST}	τ_{NAT}	τ_{GHG}	τ_{AA}	τ_{OZ}	τ_{LU}	<i>PP</i>	τ_{HIST}	τ_{NAT}	τ_{GHG}	τ_{AA}	τ_{OZ}	τ_{LU}
MMoM														
ACCESS1-3														
BCC-CSM1-1														
CanESM2														
CCSM4														
CMCC-CESM														
CNRM-CM5														
CSIRO_Mk3-6-0														
FGOALS-g2														
GFDL-ESM2M														
GISS-E2H														
HadGEM2-CC														
HadGEM2-ES														
INMCM4														
IPSL-CM5A-LR														
MIROC4h														
MIROC5														
MIROC-ESM														
MPI-ESM-LR														
MRI-CGCM3														
NorESM1-M														

Note: τ_{HIST} column: simulations with τ of the same (opposite) sign as (to) GPCP's are shaded blue (red), with those distinguishable from natural internal variability (5th to 95th confidence interval of *R* distribution against PICONTR0L) crossed. Other columns: simulations with τ not distinguishable from natural internal variability are shaded grey; those with τ distinguishable from internal natural variability and in agreement (opposite) with (to) GPCP's trend sign are shaded blue (red). Unshaded cells do not have simulations for the scenario.

and Shimizu (2012), who identified an adequate performance of HadGEM2-ES in simulating the SACZ dipole, and Jones and Carvalho (2013), who identified GFDL-ESM2M and MIROC4h as the models with more realistic simulations of the SAMS characteristics. MIROC4h, in addition to MIROC-ESM and INMCM4, were also identified as agreeing with the observed precipitation over subtropical South America by Barros and Doyle (2018). The models mentioned in those studies are among those correctly simulating the precipitation rate over SEBr and SESA (Table 4).

4 | PRECIPITATION TREND IN RECENT DECADES

Consistently with Zilli *et al.* (2017; 2019), GPCP τ (1979–2019) is negative over the SACZ and positive to its south

(shades in Figure 1a). In addition to being significant against the Mann–Kendall trend test (stippling in Figure 1a), the trends observed over SEBr and SESA are not within the 5th–95th percentile range defined by the PICONTR0L distribution and thus are distinguishable from internal natural variability (red cross-hatching in Figure 1a). There is also significant decrease (increase) in *PP* over southern (western) Amazon and the northern coast of SA since 1979, which has also been identified in previous observational studies (Marengo, 2004; Espinoza *et al.*, 2019).

We also tested GPCP τ considering only the period in common with CMIP5 (1979–2005; Figure 1b). The resulting trends are similar, with a reduction in precipitation over the continental SACZ extending toward southern Amazon and over the northern coast of South America. However, the spatial pattern of wetting trends over SESA is not evident yet. The magnitude of the trends

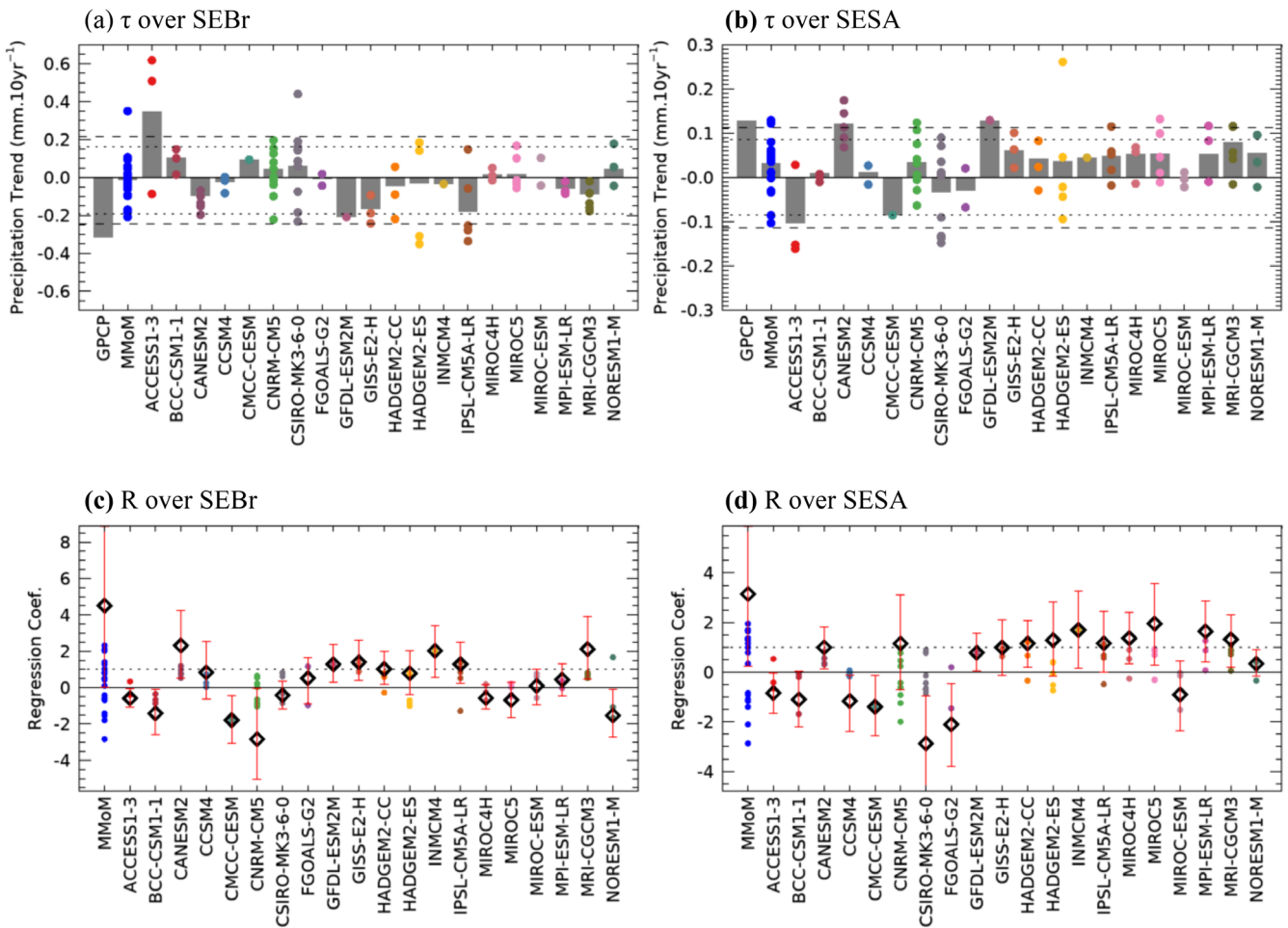


FIGURE 4 (a,b) Spatially averaged τ for GPCP, MMoM, each MMeM (bars) and individual members (dots; in MMoM dots represent each MMeM) in the HIST scenario. Dashed (dotted) lines: 5th–95th (10th–90th) confidence interval defined by the PICONTR0L scenario. (c,d) R (from Equation (5)) between GPCP and MMoM, each MMeM, and individual members (dots). Red bars with whiskers: Confidence interval (5th–95th percentile) defined by the regression of MMoM and each MMeM onto all 40-year PICONTR0L periods. Values are averaged over (a) and (c) SEBr and (b) and (d) SESA [Colour figure can be viewed at wileyonlinelibrary.com]

over both study areas is smaller and not significant. The lack of significant trends over this reduced period reinforces the need of extending the analysis until 2019 and include important variabilities observed after 2005. Thus, we will focus on the 40-year period (1979–2019) for the remainder of the analysis.

Over SEBr (SESA), the spatial average of GPCP τ (considering the 40-year period) indicates a reduction (increase) of $-0.32 \text{ mm}\cdot\text{day}^{-1}$ per decade ($+0.13 \text{ mm}\cdot\text{day}^{-1}$ per decade) in the precipitation rate since 1979 (Table 3 and Figure 4a,b). Both values are outside the 5th–95th percentile confidence interval defined by the PICONTR0L distribution (dotted lines in Figure 4a,b) and thus cannot be attributed to natural internal variability. Gonzalez *et al.* (2013) found a similar magnitude of trends over SESA when considering precipitation rates from gridded datasets and individual stations.

Despite being able to correctly reproduce the DJF precipitation rate, CMIP5 HIST simulations (considering the 40-years period between 1966–2005) are less accurate in reproducing τ (Figure 1c). The MMoM simulation correctly places positive trends over western Amazon and the southern portion of SA. However, over both study areas, τ_{HIST} has the same sign as in GPCP, but its spatial average is close to zero (Figure 4a,b and Table 3). Consequently, the value of R is large ($=4.51$ and 3.15 over SACZ and SESA, respectively; Figure 4c,d), indicating the underestimation of the precipitation trend by the MMoM. The large spread between the 5th and the 95th percentiles (MMoM error bar in Figure 4c,d) is also a consequence of the small values of τ_{HIST} . Note that the error bar is estimated by Equation (5), with τ_{HIST} in each grid point as $x_{i,s}$ and the τ estimated in each PICONTR0L realization as

$x_{i,0}$. Despite the small magnitude of τ_{HIST} , the lower limit of the confidence interval of MMoM's R is above zero, suggesting that the spatial pattern of τ_{HIST} cannot be considered similar to those obtained in the PICONTR0L simulations and cannot be explained by internal natural variability alone.

The small magnitude of the trends simulated by the MMoM and the large spread of its confidence interval is an outcome of the large discrepancies among MMeMs (dots in Figure 4a,b). Over SEBr, the spatially averaged τ_{HIST} is negative in 11 of the 20 MMeM (Figure 4a and Table 4) and 44 of the 76 members. However, only one MMeM and 11 members simulated negative and significant τ_{HIST} (considering a 10th to 90th percentile confidence interval; dotted line in Figure 4a). The MMeMs that better simulate the intensity of τ_{HIST} are those with good agreement among their members: CanESM2M, GFDL-ESM2M, GISS-E2-H (despite its poor representation of PP), INMCM4, IPSL-CM5A-LR, and MRI-CGCM3 (Figure 4a). In these models, τ_{HIST} is more intense over land (Figure 3), resulting in values of R close to unity (Figure 4c). Furthermore, the confidence interval of R in these MMeMs is above 0, indicating that the spatial pattern of these trends cannot result solely from natural internal variability.

Over SESA, the spatially averaged value of τ_{HIST} is positive in 15 of the 20 MMeM (Figure 4b and Table 4) and 50 of the 76 members. However, all except two MMeMs (CanESM2 and GFDL-ESM2-M) underestimate the magnitude of τ_{HIST} (Figure 4b), resulting in non-significant trends. Similar underestimation of trends by CMIP5 historical scenarios over the region has been noticed in previous studies (Gonzalez *et al.*, 2013; Vera and Díaz, 2015; Zhang *et al.*, 2016). In addition to CanESM2 and GFDL-ESM2M, 6 other MMeMs correctly simulate the spatial pattern of τ_{HIST} (R values close to 1 in Figure 4d), although with underestimated magnitude (HadGEM2-CC, INMCM4, MIROC4h, MIROC5, MPI-ESM-LR, and MRI-CGCM3). In these eight MMeMs, the spatial pattern of the trends over SESA cannot be attributed to natural internal variability (Figure 4d). Note, however, that CanESM2 and MPI-ESM-LR MMeMs have the worst performance in simulating PP over this study area.

Hence, the HIST scenarios of MMoM and a part of the MMeMs simulate spatial patterns of precipitation trends that are similar to those observed in GPCP and with a spatial pattern that cannot be attributed to internal natural variability alone. However, the large variability among MMeM and their members results in an underestimation of the precipitation trends' magnitude over both study areas. The large variability among individual members suggests that the simulations may fail to correctly reproduce the mechanisms associated with the

observed precipitation changes. It is also important to recall that the CMIP5 simulations end in 2005 and does not capture important changes in precipitation in the last decade. Nonetheless, the spatial analysis suggests that the simulated spatial pattern of the precipitation trends is similar to the observed pattern and is already detectable by some of the individual members.

5 | ATTRIBUTION ANALYSIS

To further investigate whether the observed trends are related to natural external variability (such as changes in solar radiation or volcanic emissions) or are a response to anthropogenic forcings, we repeat the previous analysis considering CMIP5 individual forcing scenarios. The natural external forcing is represented by the NAT scenario while anthropogenic forcings are divided into GHG emissions (GHG scenario), anthropogenic aerosols (AA), changes in ozone (OZ), and land-use changes (LU). The climatology of each MMoM scenario is similar to the HIST MMoM and GPCP (Table 3) and will not be further discussed. In this part of the analysis, we focus on analysing whether the simulated spatial pattern of the trends is distinguishable from natural internal variability.

Natural external forcings (NAT scenario) result in weak negative τ_{NAT} over most of SA (Figure 5b). Small areas with positive trends can be found over the ITCZ and the SESA (including the study area). The magnitude of the simulated values of τ_{NAT} spatially averaged over SEBr (SESA) are negative (positive) but not significant when compared to the PICONTR0L (Figure 6a,b). The small magnitude of τ_{NAT} in MMoM and MMeM results from the lack of agreement among members (Figure 6) and is an indication of the large uncertainties regarding the effects of natural external forcings in the precipitation rate over the study regions. Despite their small magnitude, the spatial pattern of τ_{NAT} are significantly different from natural internal variability (5th–95th confidence interval for R does not include zero) in the MMoM and about half of the MMeM (Figure 6c,d, and Table 4). Among the MMeM with trends significantly different from natural internal variability, 6 of them simulate τ_{NAT} with a spatial pattern similar to the observed τ , with negative trends over the SEBr and positive ones in SESA (Figure 6a,b and Table 4). However, the small magnitude of the forcings (volcanic activity and very minor changes in insolation over the period considered) suggest that part of the trends in this scenario could be resulting from internal variability.

Among the anthropogenic forcings, changes in anthropogenic greenhouse gases (GHG) result in small and positive precipitation trends (τ_{GHG}) over most of

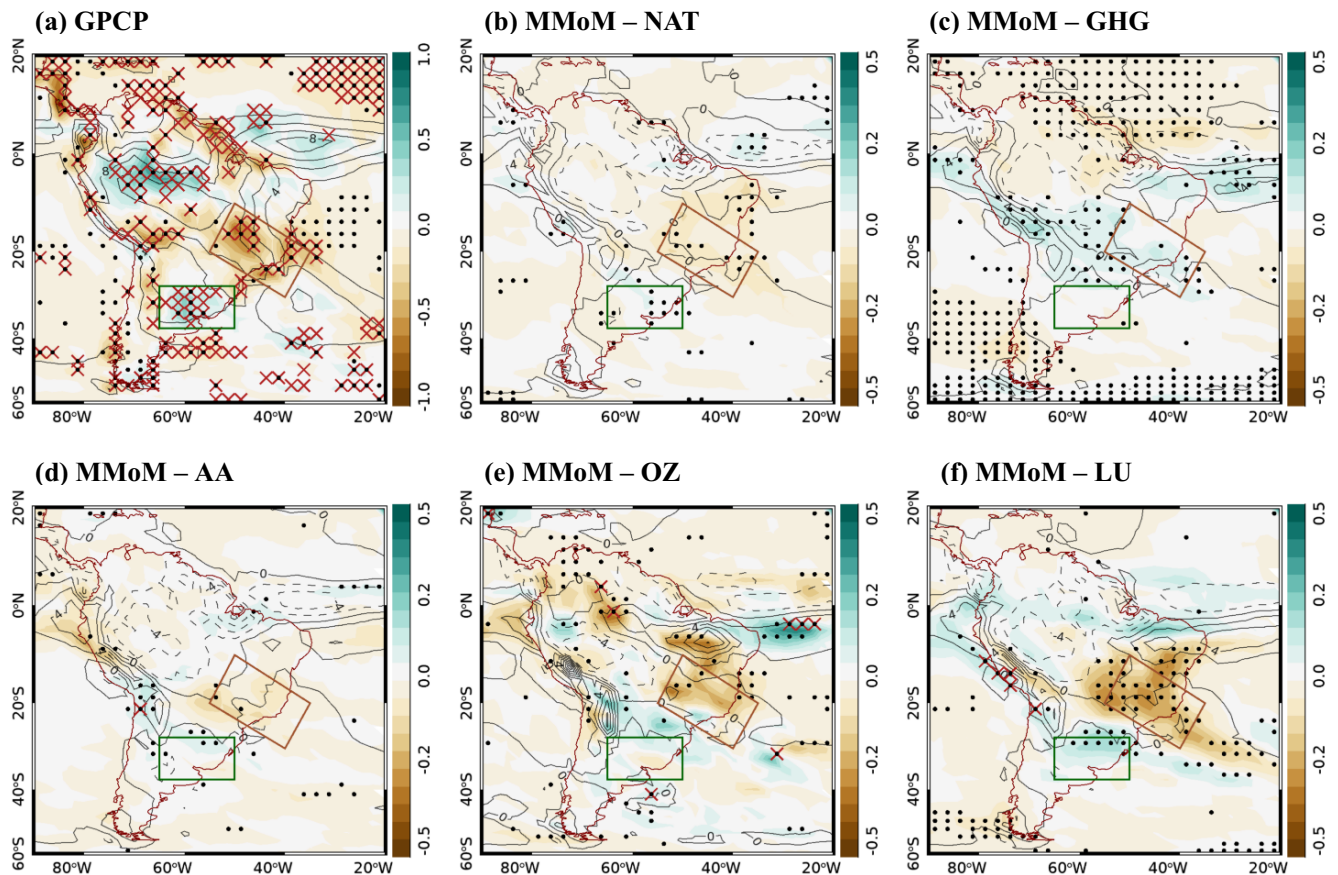


FIGURE 5 As in Figure 1 for (a) GPCP and MMoM of the (b) NAT, (c) GHG, (d) AA, (e) OZ, and (f) LU scenarios. Note reduced Sen's slope range in (b)–(f) [Colour figure can be viewed at wileyonlinelibrary.com]

central and subtropical SA in the MMoM (Figure 5c). Over SEBr, τ_{GHG} simulated by the MMoM is positive but indistinguishable from natural internal variability (Figure 6a). Since MMoM τ_{GHG} is opposite to the GPCP's trend, R is negative and the spatial pattern of τ_{GHG} is distinguishable from natural internal variability over the area (Figure 6c). However, the disagreement among individual MMeMs is large, with 5 (3) of the 12 MMeMs (Figure 6c and Table 4) and 13 (10) of the 41 members simulating positive (negative) values of τ_{GHG} with spatial pattern that cannot be attributed to natural internal variability. Over SESA, τ_{GHG} is close to zero and its spatial pattern is not distinguishable from natural internal variability in the MMoM (Figure 6b, d). Furthermore, τ_{GHG} is not significant in any of the MMeM (Figure 6b), despite having spatial patterns that are not attributable to natural internal variability in some cases (Figure 6d and Table 4). Thus, due to the large uncertainties in simulating the responses of precipitation to changes in GHG concentration, their influence on the observed precipitation rate over SEBr and SESA cannot be attributed to GHG in the current set of models.

The small magnitude of τ in the GHG scenario suggests the importance of other anthropogenic forcings. Among

the scenarios considered here, changes in land use (LU) result in the largest values of τ_{LU} (Figure 6a,b), with drying (wetting) trends over central-eastern Brazil (SESA) and extending along the northern (southern) margin of the MMoM SACZ (Figure 5f), similar to the observed τ . The influence of LU is stronger over SEBr where the spatial pattern of τ_{LU} is distinguishable from natural internal variability in the MMoM and all MMeMs (Figure 6c). In 2 of the 3 MMeMs and 4 of the 8 members, the simulated τ_{LU} is similar to GPCP's (R close to 1 in Figure 6c and Table 4). Over SESA, the spatial pattern of τ_{NAT} is not attributable to internal natural variability in the MMoM, 2 of the 3 MMeMs and 2 of the 8 members (Figure 6d and Table 4).

Changes in tropospheric and stratospheric ozone (OZ) and anthropogenic aerosol (AA) also result in similar wetting/drying trends over SA, more intense over the SEBr (Figure 5d,e, respectively), where the spatial pattern of both τ_{OZ} and τ_{AA} in the MMoM are distinguishable from natural internal variability (Figure 6c). Over this region, τ_{OZ} has the second-largest value ($-0.1 \text{ mm} \cdot \text{day}^{-1}$ per decade; Table 3 and Figure 6a), but this scenario has only one MMeM with 2 members (CCSM4). The influence of changes in AA over SEBr is not as pronounced, resulting in a spatial

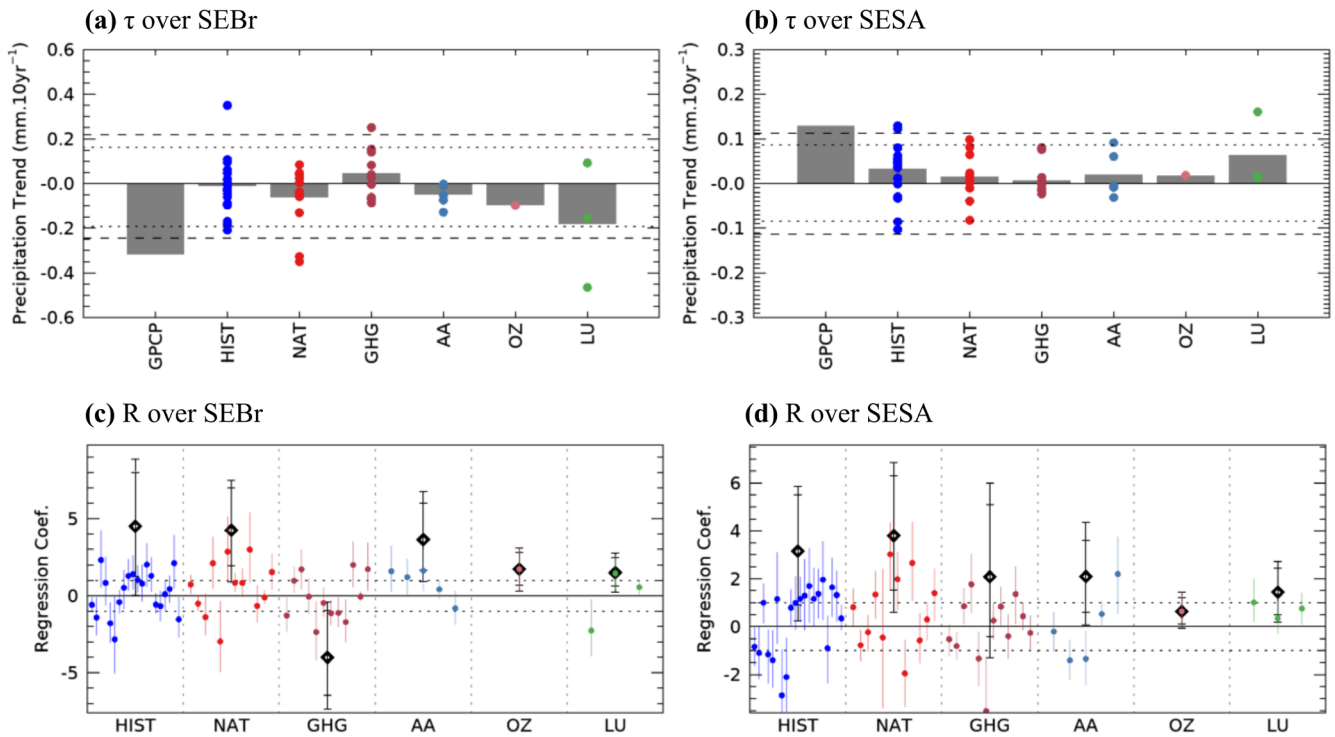


FIGURE 6 (a,b) Spatially averaged τ for GPCP, MMoM (bars) and each MMeM (dots) in each scenario. Dashed (dot) lines represent the 5th-95th (10th-90th) confidence interval defined by the PICONTR0L scenario. (c,d) R (from Equation (5)) between GPCP and MMoM (diamonds), and each MMeM (dots) for each scenario. Black bars with whiskers (colour bars): 5th-95th confidence interval defined by the regression of MMoM (each MMeM) onto all 40-year PICONTR0L periods. Values are averaged over (a) and (c) SEBr and (b) and (d) SESA [Colour figure can be viewed at wileyonlinelibrary.com]

average of MMoM τ_{AA} of $-0.05 \text{ mm}\cdot\text{day}^{-1}$ per decade (Table 3), which is similar in magnitude (but opposite sign) to the trends resulting from the NAT scenario (Figure 6a). Despite the small magnitude of τ_{AA} , this is the scenario with the largest agreement among individual members, with all MMeM (Figure 6a) and 15 of the 20 members simulating negative trends over the area. The spatial pattern of τ_{AA} can be considered significantly different from natural internal variability in 2 of the 5 MMeMs (Figure 6c and Table 4) and 9 of 20 members. Over SESA, the spatial pattern of τ_{OZ} and τ_{AA} simulated by MMoM are distinguishable from natural internal variability only when considering the 10th-90th confidence interval from PICONTR0L distribution. MMoM τ_{AA} is small due to the lack of agreement among the MMeMs and individual members (Figure 6d). In OZ scenario, the spatial pattern of the τ_{OZ} is distinguishable from natural variability in only one member.

6 | DISCUSSION

6.1 | Detection of precipitation trends

Observational studies have indicated a poleward shift in the SACZ-related summer precipitation rate in recent

decades (Zilli *et al.*, 2017; 2019). Similar changes have also been identified in future projections of climate change (Seth *et al.*, 2010; Junquas *et al.*, 2013; Talento and Barreiro, 2017). In the present analysis, the historical simulations from MMoM and part of the 20 MMeM correctly simulate the DJF the precipitation rate over the SACZ, even though with maximum precipitation located to the north of its observed position. This affects the SACZ-related precipitation dipole, resulting in an underestimation of the precipitation rate and trend over SESA, as already described in previous studies (Gulizia and Camilloni, 2015; Vera and Díaz, 2015; Barros and Doyle, 2018). Over SEBr, the large uncertainties among the MMeMs and individual members of each ensemble result in the lack of significant trend in the MMoM. However, it is important to emphasize the different period of analysis, with MMoM not capturing important precipitation trends observed after 2005. The bias observed in precipitation rates over both areas could suggest that the models are not able to correctly reproduce the mechanisms related to the location and intensity of the SACZ (and related SACZ-dipole).

Despite the small magnitude, the spatial pattern of the simulated HIST precipitation trend indicates a drying (wetting) trend over SEBr (SESA) coherent with trends in

the SACZ dipole observed in Zilli *et al.* (2017; 2019). Previous studies, based on filtered precipitation analysis (such as EOF), have identified similar historical and future changes in the SACZ-related dipole (Junquas *et al.*, 2013; Díaz and Vera, 2017). Our results indicate a simulated spatial pattern of precipitation trends that cannot be attributed to internal natural variability alone and are consistent with the future projections. However, the large variability among MMeM and individual members of each MMeM increases the uncertainties regarding the magnitude of the trends.

6.2 | Attribution analysis

While large uncertainties among individual members reduce our ability to conclusively attribute the observed trends to a set of forcings, the emerging patterns from each individual scenario allows a qualitative assessment of the influence of anthropogenic forcings in the local precipitation trends. Land-use change is the main forcing associated with the reduction (increase) in precipitation rates over SEBr (SESA), followed by anthropogenic-related changes in stratospheric and tropospheric ozone contributing to the reduction in precipitation rate over SEBr.

According to the present analysis, changes in land use result in the largest contribution to the simulated changes in precipitation over both study areas. Even though the present analysis does not indicate the location of this forcing, whether it is local (e.g., in the La Plata Basin [LPB], where the largest part of both study regions are located) or remote (in the Amazon Basin), changes in land use could affect the SACZ-related precipitation. The Amazon region is one of the main sources of moisture to the SACZ and SESA (Arraut *et al.*, 2012). The transport of moisture to the SACZ depends strongly on the characteristics of the Low-Level Jet (LLJ) east of the Andes (Arraut and Satyamurty, 2009; Nascimento *et al.*, 2016; Montini *et al.*, 2019). Changes in land use in the Amazon, mainly associated with deforestation, may reduce the amount of moisture recycling, affecting precipitation in the region (Zemp *et al.*, 2017a) and reducing the amount of moisture transported by the LLJ toward the SACZ and the SESA (Zemp *et al.*, 2017b).

Over the LPB, changes in land use since 1950s have reduced the area of native vegetation (mostly savanna and forest) to less than 20% (Tucci and Clarke, 1998). The conversion of native vegetation to crop land can result in drier surface conditions that can modify the thermal structure of the atmosphere, affecting the low level circulation, consequently, the moisture transport toward SACZ and SESA (Lee and Berbery, 2012; Yang and Dominguez, 2019). Using simulations from Weather

Research and Forecast Model (WRF) experiments, Lee and Berbery (2012) demonstrated that land-use changes within the LPB are associated with a reduction (increase) in precipitation over the northern (southern) part of the basin. According to them, land-use changes from native vegetation to dry crops increases the albedo and decreases the surface friction over the northern part of the basin, reducing the sensible heat flux and near-surface temperature, which in turn reduces convective instability over the region. Additionally, the reduction in surface roughness accelerates the surface winds favouring moisture divergence over the area and reducing precipitation. Further south, land-use changes from native grassland to dry crops have the opposite effect, mostly due to a reduction in albedo, resulting in increased precipitation. The spatial pattern of changes in precipitation described by these authors is similar to those observed in GPCP and simulated by the LU MMeM, suggesting that changes in land use over central and southeastern SA could be affecting the surface processes associated with the strength and location of the SACZ-related precipitation dipole.

In addition to changes in land use, anthropogenic forcings related to changes in the concentration of ozone also contribute to precipitation trends, albeit with small intensity. Previous studies suggest that ozone depletion is associated with a poleward expansion of the Hadley cell in the Southern Hemisphere and a consequent shift in the jet position, which would result in increased precipitation over SESA (Polvani *et al.*, 2011; Gonzalez *et al.*, 2014). The position of the subtropical jet is one of the ingredients necessary for the development of the SACZ over eastern Brazil, advecting negative vorticity and favouring upper-level divergence over the region (Kodama, 1992; 1993). Thus, a poleward shift of the jet could also affect the location and intensity of the SACZ, resulting in the drying (wetting) trends in the SACZ north (southern) flank, consistent with Zilli *et al.* (2019).

Finally, the response of the precipitation to changes in GHG cannot be distinguishable from natural internal variability. The lack of consensus regarding the sign of the trend suggests that internal variability dominates trends in this scenario.

6.3 | Other factors associated with the observed trends

Another source of discrepancies between observed and simulated trends is related to the position of the SACZ in CMIP5 models. The present analysis is based on fixed study regions located over areas with large observed precipitation trends. However, some CMIP5 models simulate

the SACZ displaced to the north of its climatological position, resulting in trends outside the study regions. The utilization of approaches based on the location of the SACZ in each model could improve the identification of the forcings and mechanisms associated with the observed changes, without being restricted to models that accurately reproduce the SACZ's location.

Despite demonstrating that the detected precipitation trends cannot be caused by internal variability alone, trends resulting from NAT forcings suggest that at least part of the changes in the position and intensity of the SACZ could be associated with changes in climatic modes. The analysis period, 1979–2019, encompasses a transition from cold to warm AMO phase, which possibly contributes to the precipitation trends over the study region (Chiessi *et al.*, 2009; Grimm and Saboia, 2015; Jones and Carvalho, 2018; Kayano *et al.*, 2019). A previous study (Zhang and Wang, 2013) demonstrated that the AMO transition from cold to warm phase occurred between 1975 and 2005 in all CMIP5 models analysed, even though most of them are not able to correctly represent the spatial structure and intensity of the mode. Thus, it is possible that the AMO have influenced the observed trends and that the lack of agreement among the CMIP5 simulations arises from a misrepresentation of the influence of this mode on the SACZ-related dipole. A more in-depth evaluation of the topic should also include other variables, such as circulation and sea surface temperature, which will be addressed in future research.

7 | CONCLUSIONS

The present analysis indicates that precipitation trends observed over the SACZ and SESA regions over the last 40 years consistent with Zilli *et al.* (2019) are detectable in some of the historical simulations of the CMIP5 climate models. The results indicate large disagreement among individual models, suggesting that the mechanism related to the observed precipitation trends are not well represented in the selected models. The large uncertainties prevent a robust attribution analysis of the main forcings. Nonetheless, a qualitative assessment of the results suggests that part of the precipitation trends over SEBr and SESA could result from changes in land-use and anthropogenic-related stratospheric and tropospheric ozone concentration.

The results focus only on changes in daily average precipitation rate during austral summer (DJF) based on robust statistical analyses. However, a careful consideration of mechanisms driving the observed and simulated changes in precipitation is also important to assess climate projections over the region, particularly along transition zones such as

the SACZ, where the uncertainty in simulations is large (Carvalho and Jones, 2013; Jones and Carvalho, 2013; Sanchez *et al.*, 2015; de Barros Soares *et al.*, 2017; Díaz and Vera, 2017). Over the SACZ, the number of rainy days is decreasing (Zilli *et al.*, 2017) likely due to weaker northerly winds along the eastern Brazilian coast and reduced available moisture in the lower-to-mid troposphere (Zilli *et al.*, 2019). On the other hand, the intensity of extreme events is increasing over the same region (Zilli *et al.*, 2017), suggesting the importance of the combined influence of dynamic and thermodynamic forcings on the observed changes (Chen *et al.*, 2019; Norris *et al.*, 2019a, 2019b). Thus, besides correctly reproducing the observed average precipitation trends, it is necessary to assess the accuracy of the CMIP5 models in reproducing the observed trends in extreme precipitation, as well as dynamic and thermodynamic forcings associated with the intensification of these events.

ACKNOWLEDGEMENTS

GPCP Precipitation data was provided by the NOAA/OAR/ESRL PSL, Boulder, Colorado, USA, from their website at <https://psl.noaa.gov/>. All CMIP5 data was downloaded from the PCMDI website at <http://pcmdi9.llnl.gov/>. The authors acknowledge the World Climate Research Program's Working Group on Coupled Modelling, which is responsible for CMIP, and we thank the climate modelling groups (listed in Table 1 of this paper) for producing and making available their model output. M. Zilli acknowledges the Brazilian National Council for Scientific and Technological Development (CNPq) for the financial support through the Science without Borders Program (202691/2011-0). L. Carvalho acknowledges the support of NSF-AGS-1505198.

ORCID

Marcia T. Zilli  <https://orcid.org/0000-0003-1670-8567>

REFERENCES

- Adler, R., Wang, J.-J., Sapiano, M., Huffman, G., Chiu, L., Xie, P.-P., Ferraro, R., Schneider, U., Becker, A., Bolvin, D., Nelkin, E., Gu, G. and NOAA CDR Program. (2016) *Global Precipitation Climatology Project (GPCP) Climate Data Record (CDR), Version 2.3 (Monthly)*. National Centers for Environmental Information. <https://doi.org/10.7289/V56971M6> [Accessed in 8th March 2020].
- Adler, R.F., Sapiano, M.P.R., Huffman, G.J., Wang, J.-J., Gu, G., Bolvin, D., Chiu, L., Schneider, U., Becker, A., Nelkin, E., Xie, P., Ferraro, R. and Shin, D.-B. (2018) The global precipitation climatology project (GPCP) monthly analysis (new version 2.3) and a review of 2017 global precipitation. *Atmosphere*, 9, 138. <https://doi.org/10.3390/atmos9040138>.
- Arora, V.K., Scinocca, J.F., Boer, G.J., Christian, J.R., Denman, K. L., Flato, G.M., Kharin, V.V., Lee, W.G. and Merryfield, W.J. (2011) Carbon emission limits required to satisfy future representative concentration pathways of greenhouse gases.

- Geophysical Research Letters*, 38, L05805. <https://doi.org/10.1029/2010GL046270>.
- Arraut, J., Nobre, C., Barbosa, H., Obregon, G. and Marengo, J. (2012) Aerial rivers and lakes: looking at large-scale moisture transport and its relation to Amazonia and subtropical rainfall in South America. *Journal of Climate*, 25, 543–556. <https://doi.org/10.1175/2011JCLI4189.1>.
- Arraut, J.M. and Satyamurty, P. (2009) Precipitation and water vapor transport in the southern hemisphere with emphasis on the south American region. *Journal of Applied Meteorology and Climatology*, 48, 1902–1912. <https://doi.org/10.1175/2009JAMC2030.1>.
- Barkhordarian, A., von Storch, H. and Bhend, J. (2013) The expectation of future precipitation change over the Mediterranean region is different from what we observe. *Climate Dynamics*, 40, 225–244. <https://doi.org/10.1007/s00382-012-1497-7>.
- Barkhordarian, A., von Storch, H. and Zorita, E. (2012) Anthropogenic forcing is a plausible explanation for the observed surface specific humidity trends over the Mediterranean area. *Geophysical Research Letters*, 39, L19706. <https://doi.org/10.1029/2012GL053026>.
- Barros, V. and Doyle, M. (2018) Low-level circulation and precipitation simulated by CMIP5 GCMS over southeastern South America. *International Journal of Climatology*, 38, 5476–5490. <https://doi.org/10.1002/joc.5740>.
- Barros, V., Doyle, M. and Camilloni, I. (2008) Precipitation trends in southeastern South America: relationship with ENSO phases and with low-level circulation. *Theoretical and Applied Climatology*, 93, 19–33. <https://doi.org/10.1007/s00704-007-0329-x>.
- Barros, V., Gonzalez, M., Liebmann, B. and Camilloni, I. (2000) Influence of the South Atlantic convergence zone and South Atlantic Sea surface temperature on interannual summer rainfall variability in southeastern South America. *Theoretical and Applied Climatology*, 67, 123–133. <https://doi.org/10.1007/s007040070002>.
- de Barros Soares, D., Lee, H., Loikith, P.C., Barkhordarian, A. and Mechoso, C.R. (2017) Can significant trends be detected in surface air temperature and precipitation over South America in recent decades? *International Journal of Climatology*, 37, 1483–1493. <https://doi.org/10.1002/joc.4792>.
- Bentsen, M., Bethke, I., Debernard, J.B., Iversen, T., Kirkevåg, A., Seland, Ø., Drange, H., Roelandt, C., Seierstad, I.A., Hoose, C. and Kristjánsson, J.E. (2013) The Norwegian earth system model, NorESM1-M – part 1: description and basic evaluation of the physical climate. *Geoscientific Model Development*, 6, 687–720. <https://doi.org/10.5194/gmd-6-687-2013>.
- Bi, D., Dix, M., Marsland, S., O'Farrell, S., et al. (2013) The ACCESS coupled model: description, control climate and evaluation. *Australian Meteorological and Oceanographic Journal*, 63, 41–64. <https://doi.org/10.22499/2.6301.004>.
- Bombardi, R.J. and Carvalho, L.M.V. (2009) IPCC global coupled model simulations of the South America monsoon system. *Climate Dynamics*, 33, 893–916. <https://doi.org/10.1007/s00382-008-0488-1>.
- Bombardi, R.J., Carvalho, L.M.V., Jones, C. and Reboita, M.S. (2013) Precipitation over eastern South America and the South Atlantic Sea surface temperature during neutral ENSO periods. *Climate Dynamics*, 42, 1553–1568. <https://doi.org/10.1007/s00382-013-1832-7>.
- Carvalho, L.M.V. and Jones, C. (2013) CMIP5 simulations of low level tropospheric temperature and moisture over tropical Americas. *Journal of Climate*, 26, 6257–6286. <https://doi.org/10.1175/JCLI-D-12-00532.1>.
- Carvalho, L.M.V., Jones, C. and Liebmann, B. (2002) Extreme precipitation events in southeastern South America and large-scale convective patterns in the South Atlantic convergence zone. *Journal of Climate*, 15, 2377–2394. [https://doi.org/10.1175/1520-0442\(2002\)015<2377:EPEISS>2.0.CO;2](https://doi.org/10.1175/1520-0442(2002)015<2377:EPEISS>2.0.CO;2).
- Carvalho, L.M.V., Jones, C. and Liebmann, B. (2004) The South Atlantic convergence zone: intensity, form, persistence and relationships with intraseasonal to interannual activity and extreme rainfall. *Journal of Climate*, 17, 88–108. [https://doi.org/10.1175/1520-0442\(2004\)017<0088:TSACZI>2.0.CO;2](https://doi.org/10.1175/1520-0442(2004)017<0088:TSACZI>2.0.CO;2).
- Carvalho, L.M.V., Jones, C., Posadas, A.N., Quiroz, R., Bookhagen, B. and Liebmann, B. (2012) Precipitation characteristics of the south American monsoon system derived from multiple datasets. *Journal of Climate*, 25, 4600–4620. <https://doi.org/10.1175/JCLI-D-11-00335.1>.
- Carvalho, L.M.V., Silva, A.E., Jones, C., Liebmann, B., Silva Dias, P. L. and Rocha, H.R. (2011) Moisture transport and intraseasonal variability in the South America monsoon system. *Climate Dynamics*, 36, 1865–1880. <https://doi.org/10.1007/s00382-010-0806-2>.
- Cavalcanti, I.F.A. and Shimizu, M.H. (2012) Climate fields over South America and variability of SACZ and PSA in HadGEM2-ES. *American Journal of Climate Change*, 1, 132–144. <https://doi.org/10.4236/ajcc.2012.13011>.
- Chen, G., Norris, J., Neelin, J.D., Lu, J., Leung, L.R. and Sakaguchi, K. (2019) Thermodynamic and dynamic mechanisms for hydrological cycle intensification over the full probability distribution of precipitation events. *Journal of the Atmospheric Sciences*, 76, 497–516. <https://doi.org/10.1175/JAS-D-18-0067.1>.
- Chiessi, C., Mulitza, S., Pätzold, J., Wefer, G. and Marengo, J. (2009) Possible impact of the Atlantic Multidecadal Oscillation on the South American summer monsoon. *Geophysical Research Letters*, 36, L21707. <https://doi.org/10.1029/2009gl039914>.
- Chou, S., Lyra, A., Mourão, C., Dereczynski, C., Pilotto, I., Gomes, J., Bustamante, J., Tavares, P., Silva, A., Rodrigues, D., Campos, D., Chagas, D., Sueiro, G., Siqueira, G., Nobre, P. and Marengo, J. (2014) Evaluation of the eta simulations nested in three global climate models. *American Journal of Climate Change*, 3, 438–454. <https://doi.org/10.4236/ajcc.2014.35039>.
- Collins, W.J., Bellouin, N., Doutriaux-Boucher, M., Gedney, N., Halloran, P., Hinton, T., Hughes, J., Jones, C.D., Joshi, M., Liddicoat, S., Martin, G., O'Connor, F., Rae, J., Senior, C., Sitch, S., Totterdell, I., Wiltshire, A. and Woodward, S. (2011) Development and evaluation of an earth-system model – HadGEM2. *Geoscientific Model Development*, 4, 1051–1075. <https://doi.org/10.5194/gmd-4-1051-2011>.
- Cunningham, C.A.C. and Cavalcanti, I.F.A. (2006) Intraseasonal modes of variability affecting the South Atlantic convergence zone. *International Journal of Climatology*, 26, 1165–1180. <https://doi.org/10.1002/joc.1309>.
- Díaz, L.B. and Vera, C.S. (2017) Austral summer precipitation inter-annual variability and trends over southeastern South America

- in CMIP5 models. *International Journal of Climatology*, 37, 681–695. <https://doi.org/10.1002/joc.5031>.
- Dufresne, J.L., Foujols, M.A., Denvil, S., Caubel, A., Marti, O., Aumont, O., Balkanski, Y., Bekki, S., Bellenger, H., Benshila, R., Bony, S., Bopp, L., Braconnot, P., Brockmann, P., Cadule, P., Cheruy, F., Codron, F., Cozic, A., Cugnet, D., de Noblet, N., Duvel, J.P., Ethé, C., Fairhead, L., Fichefet, T., Flavoni, S., Friedlingstein, P., Grandpeix, J.Y., Guez, L., Guilyardi, E., Hauglustaine, D., Hourdin, F., Idelkadi, A., Ghattas, J., Joussaume, S., Kageyama, M., Krinner, G., Labetoulle, S., Lahellec, A., Lefebvre, M.P., Lefevre, F., Levy, C., Li, Z.X., Lloyd, J., Lott, F., Madec, G., Mancip, M., Marchand, M., Masson, S., Meurdesoif, Y., Mignot, J., Musat, I., Parouty, S., Polcher, J., Rio, C., Schulz, M., Swingedouw, D., Szopa, S., Talandier, C., Terray, P., Viovy, N. and Vuichard, N. (2013) Climate change projections using the IPSL-CM5 earth system model: from CMIP3 to CMIP5. *Climate Dynamics*, 40, 2123–2165. <https://doi.org/10.1007/s00382-012-1636-1>.
- Dunne, J.P., John, J.G., Adcroft, A.J., Griffies, S.M., Hallberg, R.W., Shevliakova, E., Stouffer, R.J., Cooke, W., Dunne, K.A., Harrison, M.J., Krasting, J.P., Malyshev, S.L., Milly, P.C.D., Philipps, P.J., Sentman, L.T., Samuels, B.L., Spelman, M.J., Winton, M., Wittenberg, A.T. and Zadeh, N. (2012) GFDL's ESM2 global coupled climate-carbon earth system models. Part I: physical formulation and baseline simulation characteristics. *Journal of Climate*, 25, 6646–6665. <https://doi.org/10.1175/JCLI-D-11-00560.1>.
- Espinoza, J.C., Ronchail, J., Marengo, J.Á. and Segura, H. (2019) Contrasting north–south changes in Amazon wet-day and dry-day frequency and related atmospheric features (1981–2017). *Climate Dynamics*, 52, 5413–5430. <https://doi.org/10.1007/s00382-018-4462-2>.
- Gent, P.R., Danabasoglu, G., Donner, L.J., Holland, M.M., Hunke, E.C., Jayne, S.R., Lawrence, D.M., Neale, R.B., Rasch, P.J., Vertenstein, M., Worley, P.H., Yang, Z. and Zhang, M. (2011) The community climate system model version 4. *Journal of Climate*, 24, 4973–4991. <https://doi.org/10.1175/2011JCLI4083.1>.
- Giorgetta, M.A., Jungclaus, J., Reick, C.H., Legutke, S., Bader, J., Böttinger, M., Brovkin, V., Crueger, T., Esch, M., Fieg, K., Glushak, K., Gayler, V., Haak, H., Hollweg, H.D., Ilyina, T., Kinne, S., Kornblueh, L., Matei, D., Mauritsen, T., Mikolajewicz, U., Mueller, W., Notz, D., Pithan, F., Raddatz, T., Rast, S., Redler, R., Roeckner, E., Schmidt, H., Schnur, R., Segschneider, J., Six, K.D., Stockhause, M., Timmreck, C., Wegner, J., Widmann, H., Wieners, K.H., Claussen, M., Marotzke, J. and Stevens, B. (2013) Climate and carbon cycle changes from 1850 to 2100 in MPI-ESM simulations for the coupled model Intercomparison project phase 5. *Journal of Advances in Modeling Earth Systems*, 5, 572–597. <https://doi.org/10.1002/jame.20038>.
- Gonzalez, P.L.M., Goddard, L. and Greene, A.M. (2013) Twentieth-century summer precipitation in south eastern South America: comparison of gridded and station data. *International Journal of Climatology*, 33, 2923–2928. <https://doi.org/10.1002/joc.3633>.
- Gonzalez, P.L.M., Polvani, L.M., Seager, R. and Correa, G.J.P. (2014) Stratospheric ozone depletion: a key driver of recent precipitation trends in South Eastern South America. *Climate Dynamics*, 42, 1775–1792. <https://doi.org/10.1007/s00382-013-1777-x>.
- Grimm, A.M. and Saboia, J. (2015) Interdecadal variability of the South American precipitation in the monsoon season. *Journal of Climate*, 28, 755–775. <https://doi.org/10.1175/JCLI-D-14-00046.1>.
- Grimm, A.M. and Zilli, M.T. (2009) Interannual variability and seasonal evolution of summer monsoon rainfall in South America. *Journal of Climate*, 22, 2257–2275. <https://doi.org/10.1175/2008JCLI2345.1>.
- Gulizia, C. and Camilloni, I. (2015) Comparative analysis of the ability of a set of CMIP3 and CMIP5 global climate models to represent precipitation in South America. *International Journal of Climatology*, 35, 583–595. <https://doi.org/10.1002/joc.4005>.
- Gupta, A.S., Jourdain, N.C., Brown, J.N. and Monselesan, D. (2013) Climate Drift in the CMIP5 Models. *Journal of Climate*, 26, 8597–8615. <https://doi.org/10.1175/JCLI-D-12-00521.1>.
- Haylock, M.R., et al. (2006) Trends in total and extremes south American rainfall in 1960–2000 and links with sea surface temperature. *Journal of Climate*, 19, 1490–1512. <https://doi.org/10.1175/JCLI3695.1>.
- Hegerl, G. and Zwiers, F. (2011) Use of models in detection and attribution of climate change. *WIREs Climate Change*, 2, 570–591. <https://doi.org/10.1002/wcc.121>.
- Jeffrey, S.J., Rotstain, L.D., Collier, M.A., Dravitzki, S.M., Hamalainen, C., Moeseneder, C., Wong, K.K. and Syktus, J.I. (2013) Australia's CMIP5 submission using the CSIRO Mk3.6 model. *Australian Meteorological and Oceanographic Journal*, 63, 1–13.
- Jones, C. and Carvalho, L.M.V. (2002) Active and break phases in the south American monsoon system. *Journal of Climate*, 15, 905–914. [https://doi.org/10.1175/1520-0442\(2002\)015<0905:AABPIT>2.0.CO;2](https://doi.org/10.1175/1520-0442(2002)015<0905:AABPIT>2.0.CO;2).
- Jones, C. and Carvalho, L.M.V. (2013) Climate change in the south American monsoon system: present climate and CMIP5 projections. *Journal of Climate*, 26, 6660–6678. <https://doi.org/10.1175/JCLI-D-12-00412.1>.
- Jones, C. and Carvalho, L.M.V. (2018) The influence of the Atlantic Multidecadal Oscillation on the eastern Andes low-level jet and precipitation in South America. *Nature Climate and Atmospheric Science*, 1, 40. <https://doi.org/10.1038/s41612-018-0050-8>.
- Jones, C.D., Hughes, J.K., Bellouin, N., Hardiman, S.C., Jones, G.S., Knight, J., Liddicoat, S., O'Connor, F.M., Andres, R.J., Bell, C., Boo, K.O., Bozzo, A., Butchart, N., Cadule, P., Corbin, K.D., Doutriaux-Boucher, M., Friedlingstein, P., Gornall, J., Gray, L., Halloran, P.R., Hurtt, G., Ingram, W.J., Lamarque, J.F., Law, R. M., Meinshausen, M., Osprey, S., Palin, E.J., Parsons Chini, L., Raddatz, T., Sanderson, M.G., Sellar, A.A., Schurer, A., Valdes, P., Wood, N., Woodward, S., Yoshioka, M. and Zerroukat, M. (2011) The HadGEM2-ES implementation of CMIP5 centennial simulations. *Geoscientific Model Development*, 4, 543–570. <https://doi.org/10.5194/gmd-4-543-2011>.
- Junquas, C., Vera, C.S., Li, L. and LeTreut, H. (2012) Summer precipitation variability over southeastern South America in a global warming scenario. *Climate Dynamics*, 38, 1867–1883. <https://doi.org/10.1007/s00382-011-1141-y>.
- Junquas, C., Vera, C.S., Li, L. and LeTreut, H. (2013) Impact of projected SST changes on summer rainfall in Southeastern South America. *Climate Dynamics*, 40, 1569–1589. <https://doi.org/10.1007/s00382-013-1695-y>.

- Kayano, M.T., Andreoli, R.V., Garcia, S.R. and Souza, R.A.F. (2019) How the two nodes of the tropical Atlantic Sea surface temperature dipole relate the climate of the surrounding regions during austral autumn. *International Journal of Climatology*, 38:3927–3941, 3927–3941. <https://doi.org/10.1002/joc.5545>.
- Kodama, Y.M. (1992) Large-scale common features of subtropical precipitation zones (the Baiu frontal zone, the SPCZ and the SACZ) part I: characteristics of subtropical frontal zones. *Journal of the Meteorological Society of Japan*, 70, 813–835. https://doi.org/10.2151/jmsj1965.70.4_813.
- Kodama, Y.M. (1993) Large-scale common features of subtropical convergence zones (the Baiu Frontal Zone, the SPCZ and the SACZ). Part II: conditions of the circulations for generating the STCZs. *Journal of the Meteorological Society of Japan*, 71, 581–610. https://doi.org/10.2151/jmsj1965.71.5_581.
- Lee, S. and Berbery, E.H. (2012) Land cover change effects on the climate of the La Plata Basin. *Journal of Hydrometeorology*, 13, 84–102. <https://doi.org/10.1175/JHM-D-11-021.1>.
- Li, L., Lin, P., Yu, Y., Wang, B., Zhou, T., Liu, L., Liu, J., Bao, Q., Xu, S., Huang, W., Xia, K., Pu, Y., Dong, L., Shen, S., Liu, Y., Hu, N., Liu, M., Sun, W., Shi, X., Zheng, W., Wu, B., Song, M., Liu, H., Zhang, X., Wu, G., Xue, W., Huang, X., Yang, G., Song, Z. and Qiao, F. (2013) The flexible global ocean-atmosphere-land system model, grid-point version 2: FGOALS-g2. *Advances in Atmospheric Sciences*, 30, 543–560. <https://doi.org/10.1007/s00376-012-2140-6>.
- Liebmann, B., Jones, C. and Carvalho, L.M.V. (2001) Interannual variability of daily extreme precipitation events in the state of São Paulo, Brazil. *Journal of Climate*, 14, 208–218. [https://doi.org/10.1175/1520-0442\(2001\)014<0208:IVODEP>2.0.CO;2](https://doi.org/10.1175/1520-0442(2001)014<0208:IVODEP>2.0.CO;2).
- Marengo, J.A. (2004) Interdecadal variability and trends of rainfall across the Amazon basin. *Theoretical and Applied Climatology*, 78, 79–96. <https://doi.org/10.1007/s00704-004-0045-8>.
- Marengo, J.A., Liebmann, B., Grimm, A.M., Misra, V., Silva Dias, P. L., Cavalcanti, I., Carvalho, L.M., Berbery, E., Ambrizzi, T., Vera, C., Saulo, A., Nogue-Paegle, J., Zipser, E., Seth, A. and Alves, L. (2012) Review: recent developments on the South American Monsoon System. *International Journal of Climatology*, 32, 1–21. <https://doi.org/10.1002/joc.2254>.
- Martin, G.M., Bellouin, N., Collins, W.J., et al. (2011) The HadGEM2 family of Met Office Unified Model climate configurations. *Geoscientific Model Development*, 4, 723–757. <https://doi.org/10.5194/gmd-4-723-2011>.
- Mo, K. and Nogue-Paegle, J. (2001) The Pacific-south American modes and their downstream effects. *International Journal of Climatology*, 21, 1211–1229. <https://doi.org/10.1002/joc.685>.
- Montini, T.L., Jones, C. and Carvalho, L.M.V. (2019) The South America Low-level Jet: new climatology, variability and changes. *Journal of Geophysical Research: Atmospheres*, 124, 1200–1218. <https://doi.org/10.1029/2018JD029634>.
- Muza, M.N., Carvalho, L.M.V., Jones, C. and Liebmann, B. (2009) Intraseasonal and interannual variability of extreme dry and wet events over Southeastern South America and the Subtropical Atlantic during austral summer. *Journal of Climate*, 22, 1682–1699. <https://doi.org/10.1175/2008JCLI2257.1>.
- Nascimento, M., Herdies, D.L. and Souza, D. (2016) The South American water balance: the influence of low-level jets. *Journal of Climate*, 29, 1429–1449. <https://doi.org/10.1175/JCLI-D-15-0065.1>.
- Nogués-Paegle, J., Byerle, L.A. and Mo, K.C. (2000) Intraseasonal modulation of South American summer precipitation. *Monthly Weather Review*, 128, 837–850. [https://doi.org/10.1175/1520-0493\(2000\)128<0837:IMOSAS>2.0.CO;2](https://doi.org/10.1175/1520-0493(2000)128<0837:IMOSAS>2.0.CO;2).
- Nogues-Paegle, J. and Mo, K.C. (1997) Alternating wet and dry conditions over South America during summer. *Monthly Weather Review*, 125, 279–291. [https://doi.org/10.1175/1520-0493\(1997\)125<0279:AWADCO>2.0.CO;2](https://doi.org/10.1175/1520-0493(1997)125<0279:AWADCO>2.0.CO;2).
- Norris, J., Chen, G. and Neelin, J.D. (2019a) Changes in frequency of large precipitation accumulations over land in a warming climate from the CESM large ensemble: the roles of moisture, circulation, and duration. *Journal of Climate*, 32, 5397–5416. <https://doi.org/10.1175/JCLI-D-18-0600.1>.
- Norris, J., Chen, G. and Neelin, J.D. (2019b) Thermodynamic versus dynamic controls on extreme precipitation in a warming climate from the Community Earth System Model large ensemble. *Journal of Climate*, 32, 1025–1045. <https://doi.org/10.1175/JCLI-D-18-0302.1>.
- Polson, D. and Hegerl, G. (2017) Strengthening contrast between precipitation in tropical wet and dry regions. *Geophysical Research Letters*, 44, 365–373. <https://doi.org/10.1002/2016GL071194>.
- Polvani, L.M., Waugh, D.W., Correa, G.J. and Son, S. (2011) Stratospheric ozone depletion: the main driver of twentieth-century atmospheric circulation changes in the Southern Hemisphere. *Journal of Climate*, 24, 795–812. <https://doi.org/10.1175/2010JCLI3772.1>.
- Sakamoto, T.T., Komuro, Y., Nishimura, T., Ishii, M., Tatebe, H., Shiogama, H., Hasegawa, A., Toyoda, T., Mori, M., Sutezaki, T., Imada, Y., Nozawa, T., Takata, K., Mochizuki, T., Ogochi, K., Emori, S., Hasumi, H. and Kimoto, M. (2012) MIROC4h—a new high-resolution Atmosphere-Ocean coupled general circulation model. *Journal of the Meteorological Society of Japan*, 90, 325–359. <https://doi.org/10.2151/jmsj.2012-301>.
- Sanchez, E., Solman, S., Remedio, A., Berbery, H., Samuelsson, P., Rocha, R., Mourão, C., Li, L., Marengo, J., Castro, M. and Jacob, D. (2015) Regional climate modelling in CLARIS-LPB: a concerted approach towards twenty first century projections of regional temperature and precipitation over South America. *Climate Dynamics*, 45, 2193–2212. <https://doi.org/10.1007/s00382-014-2466-0>.
- Schmidt, G.A., Kelley, M., Nazarenko, L., Ruedy, R., Russell, G.L., Aleinov, I., Bauer, M., Bauer, S.E., Bhat, M.K., Bleck, R., Canuto, V., Chen, Y.H., Cheng, Y., Clune, T.L., del Genio, A., de Fainchtein, R., Faluvegi, G., Hansen, J.E., Healy, R.J., Kiang, N.Y., Koch, D., Lacis, A.A., LeGrande, A.N., Lerner, J., Lo, K.K., Matthews, E.E., Menon, S., Miller, R.L., Oinas, V., Olos, A.O., Perlwitz, J.P., Puma, M.J., Putman, W.M., Rind, D., Romanou, A., Sato, M., Shindell, D.T., Sun, S., Syed, R.A., Tausnev, N., Tsigaridis, K., Unger, N., Voulgarakis, A., Yao, M.S. and Zhang, J. (2014) Configuration and assessment of the GISS ModelE2 contributions to the CMIP5 archive. *Journal of Advances in Modeling Earth Systems*, 6, 141–184. <https://doi.org/10.1002/2013MS000265>.
- Sen, P.K. (1968) Estimates of the regression coefficient based on Kendall's Tau. *Journal of the American Statistical Association*, 63, 1379–1389. <https://doi.org/10.1080/01621459.1968.10480934>.
- Seth, A., Rojas, M. and Rauscher, S.A. (2010) CMIP3 project changes in the annual cycle of the south American Monsoon.

- Climatic Change*, 98, 331–357. <https://doi.org/10.1007/s10584-009-9736-6>.
- Skansi, M.M., Brunet, M., Sigró, J., Aguilar, E., Groening, J.A.A., Bentancur, O.J., Geier, Y.R.C., Amaya, R.L.C., Jácome, H., Ramos, A.M., Rojas, C.O., Pasten, A.M., Mitro, S.S., Jiménez, C. V., Martínez, R., Alexander, L.V. and Jones, P.D. (2013) Warming and wetting signals emerging from analysis of changes in climate extreme indices over South America. *Global and Planetary Change*, 100, 295–307. <https://doi.org/10.1016/j.gloplacha.2012.11.004>.
- Talento, S. and Barreiro, M. (2017) Control of the South Atlantic Convergence Zone by extratropical thermal forcing. *Climate Dynamics*, 50, 885–900. <https://doi.org/10.1007/s00382-017-3647-4>.
- Taylor, K.E. (2001) Summarizing multiple aspects of model performance in a single diagram. *Journal of Geophysical Research: Atmospheres*, 106(D7), 7183–7192. <https://doi.org/10.1029/2000JD900719>.
- Taylor, K.E., Stouffer, R.J. and Meehl, G.A. (2012) An overview of CMIP5 and the experiment design. *Bulletin of the American Meteorological Society*, 93, 485–498. <https://doi.org/10.1175/BAMS-D-11-00094.1>.
- Tucci, C.E.M. and Clarke, R.T. (1998) Environmental issues in the La Plata Basin. *International Journal of Water Resources Development*, 14, 157–173. <https://doi.org/10.1080/07900629849376>.
- Vera, C.S. and Díaz, L. (2015) Anthropogenic influence on summer precipitation trends over South America in CMIP5 models. *International Journal of Climatology*, 35, 3172–3177. <https://doi.org/10.1002/joc.4153>.
- Vera, C., Higgins, W., Amador, J., Ambrizzi, T., Garreaud, R., Gochis, D., Gutzler, D., Letternater, D., Marengo, J.A., Mechoso, C.R., Nogués-Paegle, J., Silva Dias, P.L. and Zang, C. (2006a) Toward a unified view of the American Monsoon System. *Journal of Climate*, 19, 4977–5000. <https://doi.org/10.1175/JCLI3896.1>.
- Vera, C., Silvestri, G., Liebmann, B. and Gonzales, P. (2006b) Climate change scenarios for seasonal precipitation in South America from IPCC-AR4 models. *Geophysical Research Letters*, 33, L13707. <https://doi.org/10.1029/2006GL025759>.
- Vichi, M., Manzini, E., Fogli, P.G., Alessandri, A., Patara, L., Scoccimarro, E., Masina, S. and Navarra, A. (2011) Global and regional ocean carbon uptake and climate change: sensitivity to a substantial mitigation scenario. *Climate Dynamics*, 37, 1929–1947. <https://doi.org/10.1007/s00382-011-1079-0>.
- Voldoire, A., Sanchez-Gomez, E., Salas y Mélia D, et al. (2013) The CNRM-CM5.1 global climate model: description and basic evaluation. *Climate Dynamics*, 40, 2091–2121. <https://doi.org/10.1007/s00382-011-1259-y>.
- Volodin, E.M., Dianskii, N.A. and Gusev, A.V. (2010) Simulating present-day climate with the INMCM4.0 coupled model of the atmospheric and oceanic general circulations. *Izvestiya, Atmospheric and Oceanic Physics*, 46, 414–431. <https://doi.org/10.1134/S000143381004002X>.
- Watanabe, M., Suzuki, T., O'ishi, R., Komuro, Y., Watanabe, S., Emori, S., Takemura, T., Chikira, M., Ogura, T., Sekiguchi, M., Takata, M., Yamazaki, D., Yokohata, T., Nozawa, T., Hasumi, H., Tatebe, H. and Kimoto, M. (2010) Improved climate simulation by MIROC5: mean states, variability, and climate sensitivity. *Journal of Climate*, 23, 6312–6335. <https://doi.org/10.1175/2010JCLI3679.1>.
- Watanabe, S., Hajima, T., Sudo, K., Nagashima, T., Takemura, T., Okajima, H., Nozawa, T., Kawase, H., Abe, M., Yokohata, T., Ise, T., Sato, H., Kato, E., Takata, K., Emori, S. and Kawamiya, M. (2011) MIROC-ESM 2010: model description and basic results of CMIP5-20C3M experiments. *Geoscientific Model Development*, 4, 845–872. <https://doi.org/10.5194/gmd-4-845-2011>.
- Wilks, D.S. (2011) Frequentist Statistical Inference. *Statistical Methods in the Atmospheric Sciences*, Vol. 100. Oxford, UK: Academic Press. 133–186. <https://doi.org/10.1016/B978-0-12-385022-5.00005-1>.
- Wu, T., Li, W., Ji, J., Xin, X., Li, L., Wang, Z., Zhang, Y., Li, J., Zhang, F., Wei, M., Shi, X., Wu, F., Zhang, L., Chu, M., Jie, W., Liu, Y., Wang, F., Liu, X., Li, Q., Dong, M., Liang, X., Gao, Y. and Zhan, J. (2013) Global carbon budgets simulated by the Beijing climate center climate system model for the last century. *Journal of Geophysical Research: Atmospheres*, 118, 4326–4347. <https://doi.org/10.1002/jgrd.50320>.
- Yang, Z. and Dominguez, F. (2019) Investigating land surface effects on the moisture transport over South America with a moisture tagging model. *Journal of Climate*, 32, 6627–6644. <https://doi.org/10.1175/JCLI-D-18-0700.1>.
- Yin, L., Fu, R., Shevliakova, E. and Dickinson, R.E. (2013) How well can CMIP5 simulate precipitation and its controlling processes over tropical South America? *Climate Dynamics*, 41, 3127–3143. <https://doi.org/10.1007/s00382-012-1582-y>.
- Yukimoto, S., Adachi, Y., Hosaka, M., Sakami, T., Yoshimura, H., Hirabara, M., Tanaka, T.Y., Shindo, E., Tsujino, H., Deushi, M., Mizuta, R., Yabu, S., Obata, A., Nakano, H., Koshiro, T., Ose, T. and Kitoh, A. (2012) A new global climate model of the meteorological research institute: MRI-CGCM3—model description and basic performance. *Journal of the Meteorological Society of Japan*, 90, 23–64. <https://doi.org/10.2151/jmsj.2012-A02>.
- Zemp, D., Schleussner, C.-F., Barbosa, H., Hirota, M., Montade, V., Sampaio, G., Staal, A., Wang-Erlandsson, L. and Ramming, A. (2017a) Self-amplified Amazon forest loss due to vegetation-atmosphere feedbacks. *Nature Communications*, 8, 14681. <https://doi.org/10.1038/ncomms14681>.
- Zemp, D., Schleussner, C.-F., Barbosa, H.M.J. and Rammig, A. (2017b) Deforestation effects on Amazon forest resilience. *Geophysical Research Letters*, 44, 6182–6190. <https://doi.org/10.1002/2017GL072955>.
- Zhang, H., Delworth, T.L., Zeng, F., Vecchi, G., Paffendorf, K. and Jia, L. (2016) Detection, attribution, and projection of regional rainfall changes on (multi-) decadal time scales: a focus on Southeastern South America. *Journal of Climate*, 29, 8515–8534. <https://doi.org/10.1175/JCLI-D-16-0287.1>.
- Zhang, L. and Wang, C. (2013) Multidecadal North Atlantic Sea surface temperature and Atlantic meridional overturning circulation variability in CMIP5 historical simulations. *Journal of Geophysical Research: Oceans*, 118(10), 5772–5791. <https://doi.org/10.1002/jgrc.20390>.
- Zhou, J. and Lau, K.M. (1998) Does a monsoon climate exist over South America? *Journal of Climate*, 11, 1020–1040. [https://doi.org/10.1175/1520-0442\(1998\)011<1020:DAMCEO>2.0.CO;2](https://doi.org/10.1175/1520-0442(1998)011<1020:DAMCEO>2.0.CO;2).
- Zhou, J. and Lau, K.M. (2001) Principal modes of interannual and decadal variability of summer rainfall over South America. *International Journal of Climatology*, 21, 1623–1644. <https://doi.org/10.1002/joc.700>.

- Zilli, M.T., Carvalho, L.M.V., Liebmann, B. and Silva Dias, M.A. (2017) A comprehensive analysis of trends in extreme precipitation over southeastern coast of Brazil. *International Journal of Climatology*, 37, 2269–2279. <https://doi.org/10.1002/joc.4840>.
- Zilli, M.T., Carvalho, L.M.V. and Lintner, B.R. (2019) The poleward shift of South Atlantic Convergence Zone in recent decades. *Climate Dynamics*, 52, 2545–2256. <https://doi.org/10.1007/s00382-018-4277-1>.

How to cite this article: Zilli MT, Carvalho LMV. Detection and attribution of precipitation trends associated with the poleward shift of the South Atlantic Convergence Zone using CMIP5 simulations. *Int J Climatol*. 2021;1–22. <https://doi.org/10.1002/joc.7007>